

GAN-based generation of realistic 3D data

A systematic review and taxonomy

André Ferreira^{1,2,3}

Jianning Li^{2,3,4}

Kelsey L. Pomykala³

Jens Kleesiek^{3,4,5}

Victor Alves¹

Jan Egger^{2,3,4,6}

¹Center Algoritmi, University of Minho, Braga, Portugal

²Computer Algorithms for Medicine Laboratory, Graz, Austria

³Institute for AI in Medicine (IKIM), University Medicine Essen, Girardetstraße 2, 45131 Essen, Germany

⁴Cancer Research Center Cologne Essen (CCCE), University Medicine Essen, Hufelandstraße 55, 45147 Essen, Germany

⁵German Cancer Consortium (DKTK), Partner Site Essen, Hufelandstraße 55, 45147 Essen, Germany

⁶Institute of Computer Graphics and Vision, Graz University of Technology, Inffeldgasse 16, 8010 Graz, Austria

Abstract

Data has become the most valuable resource in today's world. With the massive proliferation of data-driven algorithms, such as deep learning-based approaches, the availability of data is of great interest. In this context, high-quality training, validation and testing datasets are particularly needed. Volumetric data is a very important resource in medicine, as it ranges from disease diagnoses to therapy monitoring. When the dataset is sufficient, models can be trained to help doctors with these tasks. Unfortunately, there are scenarios and applications where large amounts of data is unavailable. For example, in the medical field, rare diseases and privacy issues can lead to restricted data availability. In non-medical fields, the high cost of obtaining a sufficient amount of high-quality data can also be a concern. A solution to these problems can be the generation of synthetic data to perform data augmentation in combination with other more traditional methods of data augmentation. Therefore, most of the publications on 3D Generative Adversarial Networks (GANs) are within the medical domain. The existence of mechanisms to generate realistic synthetic data is a good asset to overcome this challenge, especially in healthcare, as the data must be of good quality and close to reality, i.e. realistic, and without privacy issues. In this review, we provide a summary of works that generate realistic 3D synthetic data using GANs. We therefore outline GAN-based methods in these areas with common architectures, advantages and disadvantages. We present a novel taxonomy, evaluations, challenges and research opportunities to provide a holistic overview of the current state of GANs in medicine and other fields.

Keywords: Synthetic Data, Data Augmentation, Volumetric Medical Imaging, Generative Models, Generative Adversarial Network, Systematic Review, 3D GANs Taxonomy

Introduction

In this systematic review, we survey works that generate realistic synthetic 3D data with Generative Adversarial Networks (GANs) Goodfellow et al. [2014]. With the massive increase of data-driven algorithms, such as deep learning-based approaches, during the last years Egger et al. [2021, 2022], data is of great interest. In this context, high-quality training, validation and testing datasets are required. Unfortunately, there are scenarios and applications where large amounts of these data are unavailable. Examples can come from the medical domain, with rare diseases, leading to an insufficient amount of initial training data. Moreover, additionally in the medical field, when dealing with real patient data, privacy issues can also limit the amount of available data. This problem does not only affect the medical field, as the cost of obtaining high-quality labeled data is very high in many other fields, such as object recognition and the study of porous media Mosser et al. [2017]; Muzahid et al. [2021]. A solution to this problem can be the generation of synthetic data to perform data augmentation along with additional novel data augmentation mechanisms Shorten and Khoshgoftaar [2019]. Realistic data are highly desired, since data that imitates reality is needed, specially in the medical field. Therefore, we outline GAN-based methods in this area with common architectures, pros, cons, evaluations, challenges, research opportunities for a holistic overview of the state-of-the-art, and we also present a novel taxonomy.

1.1 Manuscript Outline

We present a systematic review on the use of GANs for the generation of volumetric data, which includes general methods such as denoising, reconstruction, segmentation, classification, and image translation, as well as specific applications such as nuclei counting. This section presents the manuscript outline, the search strategy and the research questions. The rest of this review is organized as follows.

Section 2 provides a brief explanation of GAN architecture, main purposes, advantages, and disadvantages.

Section 3 provides an overview of the works done on generating realistic 3D data with GANs and a description of the main information and statistics re-

lated to modalities, application and metrics used. In **Section 3.1** and **Section 3.2**, brief explanations of the loss functions and evaluation metrics used in the papers are given, with appropriate references if more in-depth knowledge is needed.

Section 3.3 presents the work that was considered relevant, although it does not generate volumetric data. Table 1 summarises these works. The main papers will be discussed in **Section 3.4**. All these papers are summarized in Tables 2, 3 and 4 with respect to *Modality, Medical, Dataset, Data type, Network, Loss function, Evaluation Metric, and Resolution*. Whenever possible, these tables contain references to the datasets used as well as references to lesser known concepts and architectures. All acronyms and abbreviations, if used more than once, appear at the end of the **Section 1.1**, if used only in a particular table, they appear before that table.

In **Section 3.5** we discuss the applications in the referenced papers, divided into medical and non-medical applications (Tables 5 and 6).

The final section, **Section 4**, provides a general discussion of the current state of use of GANs, the main conclusions that emerge from the review, and research opportunities that researchers could and/or should take.

To clarify, it should be noted that this is an overview focusing mainly on the use of GANs to generate volumetric data. The reason for this choice is the will to improve 3D data generation with GANs, an underdeveloped topic with great potential but which still needs further development.

Search Strategy: We performed a search in the IEEE Xplore Digital Library, Scopus, PubMed, and Web of Science with the search query ‘(“Generative Adversarial Network” OR “Generative Adversarial Networks” OR gan OR gans) AND (generation OR generative) AND (3d OR three-dimensional OR volumetric) AND data AND synthetic)’ to find specific papers on the use of GANs for volumetric data generation. Since GANs were presented in 2014 by Goodfellow et al. [2014], all papers prior to 2014 were excluded.

During the search we found 317 non-unique records, of which 161 were duplicated and 1 was published before 2014 shown by PubMed in relation to three-dimensional multicellular tumor spheroids, leaving 155 remaining papers. Based on the titles and

abstracts, we excluded 82 records that did not mention volumetric generation with GANs. We assessed the resulting 73 different papers and excluded 1 of them, which was a review paper on deep learning in pore imaging and modelling.

This resulted in a total of 72 *core papers* about generation of volumetric data using GANs, which will be covered in depth in our review. To the best of our knowledge, this is the first review that provides a detailed analysis of the published papers on the use of GANs for the generation of volumetric data. After further reading, it turned out that 14 articles did not actually use volumetric data, but we decided to mention them briefly in this review. The PRISMA diagram in Figure 1 provides a summary overview of our screening.

Note that we include all published research, not just medical applications, which is beneficial for readers from all fields who want an overview of the potential applications of volumetric data generation using GANs. We distinguish between medical and non-medical applications, which makes it easier for the reader to focus on the desired field.

Research Questions: The overall aim of this systematic review is to analyse works published between 2014 and January 2022 on the generation of volumetric data with GANs. In this regard, we defined the following main research questions for our study: 1) What are the different applications of GANs in the generation of volumetric data? 2) What are the methods most frequently or successfully employed by GANs in the generation of volumetric data? 3) What are the strengths and limitations of these methods? 4) What improvements are sought through the use of this technology?

Acronyms and Abbreviations: The following list shows the abbreviations that are used more than once throughout the review. Other abbreviations are defined directly before each table, when used only once.

- Acc — Accuracy;
- ADNI — Alzheimer’s Disease Neuroimaging Initiative;
- Adv — Adversarial loss;
- AUC — Area Under the Curve;
- CAD — Computer-Aided Design;
- CBCT — Cone-Beam Computed Tomography;

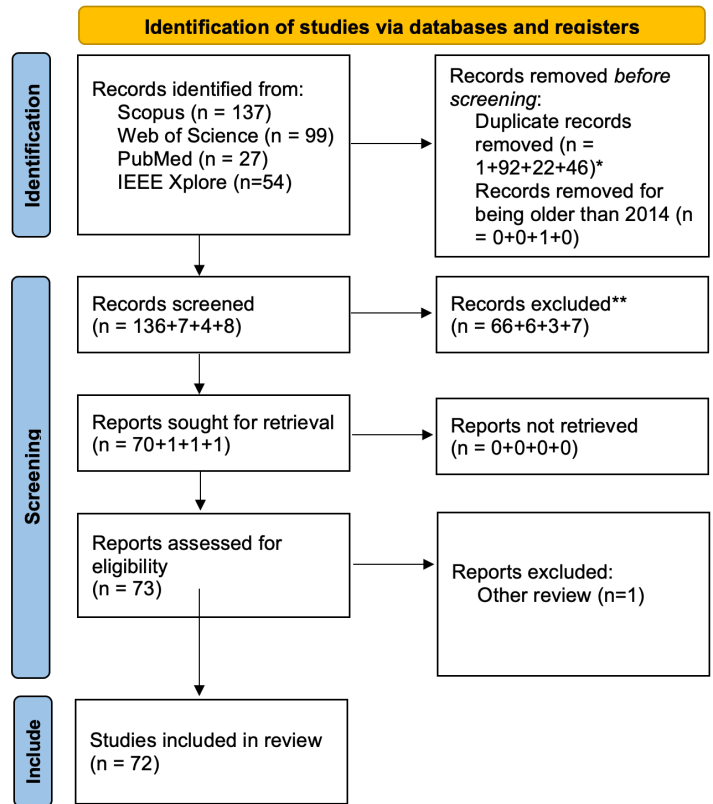


Figure 1: PRISMA diagram. *Removed using an automation tool (python script). ** Excluded because they did not involve the generation of volumetric data.

- CE — Cross-Entropy;
- cGAN — conditional GAN;
- CT — Computed Tomography;
- DCGAN — Deep Convolutional Generative Adversarial Networks;
- DSC — Dice Similarity Coefficient;
- ED-GAN — Encoder-Decoder GAN;
- FID — Fréchet Inception Distance;
- HD — Hausdorff Distance;
- HU — Hounsfield Unit;
- IoU — Intersection-over-Union;
- KL — Kullback–Leibler;
- LiDAR — Light Detection And Ranging;
- LIDC — Lung Image Database Consortium;
- LSGAN — Least Squares GAN;
- MAE — Mean Absolute Error;
- Minkowski functional — Porosity, specific surface area, average width, Euler number, Permeability;
- MRI — Magnetic Resonance Imaging;
- MSE — Mean Squared Error;
- NCC — Normalized Correlation Coefficient;
- NMSE — Normalized Mean Squared Error;
- PC — Point Cloud;
- PGGAN — Progressive Growing GANs;
- Pre — Precision;

- PSNR — Peak Signal-to-Noise Ratio;
- PTV dose — radiotherapy Planning Target Volume;
- RGB-D — Red, Green, Blue image with Depth;
- SEM — Scanning Electron Microscope;
- Sen — Sensitivity;
- Spe — Specificity;
- SSIM — Structural Similarity Index Measure;
- VTT — Visual Turing Test;
- WGAN — Wasserstein GAN;
- WGAN-GP — Wasserstein GAN with Gradient Penalty;

2 Generative Adversarial Networks

GANs were first introduced by Goodfellow et al. [2014]. They proposed a new framework in which two networks are trained to compete and overcome each other: the generator and the discriminator. The generator is trained to learn the real data distribution, i.e. it learns the distribution of the dataset and generates new synthetic data. The discriminator, which can also be called the critic, is trained to discriminate between real and synthetic data. The latter can be trained with one of two main objectives: calculate the probability of the data being real or fake, or calculate the realness or falseness of the given data (Arjovsky et al. [2017]).

Figure 2 illustrates how a vanilla GAN works. The Generator receives a random vector (Z_r) as input and generates fake data. Then the Discriminator receives fake and/or real data and returns a probability. This value is the feedback/loss that is passed on to the generator and the discriminator itself.

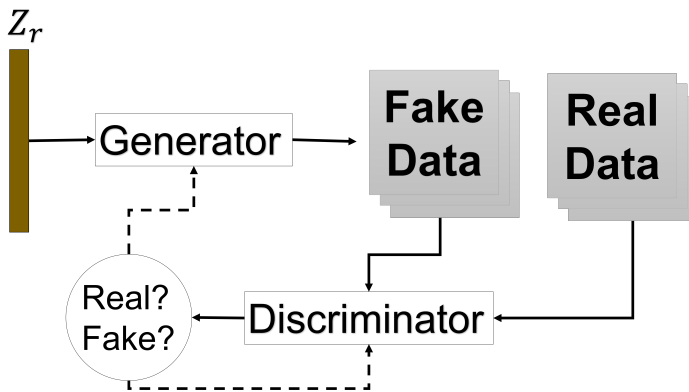


Figure 2: Illustration of the vanilla generative adversarial network (GAN). The solid lines are the data transfer and the dashed lines are the feedback/losses.

In the original work, random noise was used as input to the generator, but it can be extended to a variety of input types by using other GAN architectures, e.g. cGAN Mirza and Osindero [2014]. This allows the discriminator to receive auxiliary information, e.g. labels, in addition to synthetic and real data.

GAN training, also called "minmax game", aims to satisfy the objective Function 1, where x denotes the synthetic data, $p_z(z)$ denotes a prior input noise, $G(z)$ denotes the generated image, $D(G(z))$ denotes the probability of the fake image to be true, and $D(x)$ the probability of a real image to be true. For the cGAN, or other GAN architecture which has side information, the objective function is very similar with the original one, but $D(x) \rightarrow D(x | y)$, and $D(G(z)) \rightarrow D(G(z) | y)$, where y is the side information.

$$\min_G \max_D V(D, G) = \mathbb{E}_{x \sim p_{data}(x)} [\log(D(x))] + \mathbb{E}_{z \sim p_z(z)} [\log(1 - D(G(z)))] \quad (1)$$

However, this equation has the problem of saturation in minimising the loss of the generator $\log(1 - D(G(z)))$. To solve this problem, Goodfellow et al. [2014] propose to maximize $\log(D(G(z)))$ instead. This technique is also known as a non-saturating GAN. For more detail about the vanilla GAN and conditional GAN (cGAN), refer to Goodfellow et al. [2014]; Mirza and Osindero [2014].

2.1 Main purposes of GANs

Goodfellow et al. [2014] used GANs to improve the realism of generated images beyond what was achieved with AutoEncoders, Variational AutoEncoders and other generative models. In the last few years, GANs have been further developed with works such as Karras et al. [2018, 2019], which are capable of creating realistic human faces. The rapid progress of GANs has raised some concerns, such as the expansion and introduction of new threats and attacks, according to Brundage et al. [2018]. The report examines common artificial intelligence architectures and addresses several concerns about the security threats, for example phishing attacks or speech synthesis, which enables easier attacks on a larger scale.

Apart from these concerns, GANs enabled the development of great tools such as image-to-image translation Isola et al. [2017]; Zhu et al. [2017], text-to-image translation Zhang et al. [2017]; Dash et al.

[2017], super resolution [Ledig et al. \[2017\]](#), 3D object generation [Wang et al. \[2017\]](#), semantic translation to image [Wang et al. \[2018\]](#), removal of noise and image correction [Zhang et al. \[2019a\]](#); [Tran et al. \[2020\]](#), disentanglement using GANs [Wu et al. \[2021\]](#), among many other applications.

GANs have also improved algorithms in the medical field, mainly through their ability to generate synthetic images to train other deep learning algorithms. [Jeong et al. \[2022\]](#) provides a systematic review of medical image classification and regression and demonstrates the results that can be achieved by using these architectures. [Yi et al. \[2019\]](#) presents a more comprehensive overview of GANs in medical image analysis, highlighting the modalities and tasks.

On the other hand, our systematic review examines the use of GANs to generate volumetric data, including medical and non-medical data but properly separated for clarity. These papers report on the use of GANs for denoising, nuclei counting, reconstruction, segmentation, classification, image translation or simply general applications.

2.2 Advantages and disadvantages

The main advantages of GANs are mentioned above in [Section 2.1](#). They can be used to generate realistic data which might be used for data augmentation for other purposes, with a higher realism than other approaches. As demonstrated in [Ferreira et al. \[2022b\]](#), the use of GANs for data augmentation can outperform the use of conventional data augmentation.

One of the main concerns with this generative technology is the ability to produce deep fakes [Shen et al. \[2018\]](#); [Ponomarev \[2019\]](#) and trick detection algorithms or even humans, which can lead to misunderstandings or fraud. As evidenced by [Brundage et al. \[2018\]](#), this raises several cybersecurity concerns, as images or even fake videos can be created that are so realistic that they can fool anyone with a simple application, e.g. [Deep Fakes](#) (accessed [06-06-2022]). However, it can also be used to improve cybersecurity and combat deep fakes [Navidan et al. \[2021\]](#); [Arora and Shantanu \[2020\]](#). Although this technology permits harmful effects, the benefits that can be derived from it are immense.

In addition to the concerns mentioned above, GANs also have challenges that are more technical

([Chen \[2021\]](#)):

- **Mode collapse:** when the generator is not able to produce a large number of outputs, but always produces a small set of outputs or even the same one. This can happen when the discriminator is stuck in a local minimum and the generator learns that it is possible to produce the same set of outputs to fool the discriminator;
- **Non-convergence:** as the generator produces more and more realistic data and the discriminator cannot follow this evolution, the discriminator's feedback gradually becomes meaningless. The convergence point of the network can be characterised by the point at which the discriminator is no longer able to distinguish between real and fake data and only gives random guesses. When this point is passed, the generator is fed with poor feedback, causing the results to deteriorate;
- **Diminished gradient:** On the other hand, the feedback becomes meaningless to the generator if the discriminator performs too well. If the generator cannot improve as fast as the discriminator, or in the case of an optimal discriminator, this problem can occur;
- **Imperception:** no loss function or evaluation metric is able to mimic human judgement, which makes comparison between models very challenging without human intervention. The large-scale applications, e.g., denoising, reconstruction, synthetic data generation and segmentation, bring a lot of heterogeneity, which makes it harder to define how we can evaluate them.

2.3 Further reading

As supplementary reading, we present the following list of papers:

- [Goodfellow et al. \[2014\]](#) — Generative adversarial nets;
- [Gui et al. \[2020\]](#) — A Review on Generative Adversarial Networks: Algorithms, Theory, and Applications;

- [Kazeminia et al. \[2020\]](#) — GANs for medical image analysis;
- [Lucic et al. \[2018\]](#) Are GANs Created Equal? A Large-Scale Study.
- [Zhu et al. \[2017\]](#) — Unpaired Image-to-Image Translation using Cycle-Consistent Adversarial Networks;

These papers present how GANs work, the different ways they can be used, and the general advantages and disadvantages. They provide the reader with a deeper, but also broader, understanding of GANs, although reading them is not mandatory to understand the purpose of this review.

3 Generating realistic synthetic 3D data: a review of works

The use of GANs to generate synthetic data has increased significantly in recent years. These deep learning networks are becoming very popular, as they can generate more realistic and sharper synthetic images than other traditional generative approaches. GANs are implicit models as they do not use explicit density functions, in contrast to Variational AutoEncoders, which are explicit models [Mohamed and Lakshminarayanan \[2016\]](#). Several review articles have been submitted on the use of GANs for different purposes, ranging from more general review articles, e.g. [Alqahtani et al. \[2021\]](#), to more specific articles, e.g. [Apostolopoulos et al. \[2022\]](#).

In this review, we have refrained from providing redundant explanations of how GANs work and the main issues, as these are easy to find, and also from extending the explanations of loss functions and valuation metrics. Instead, we will give a brief explanation of each metric and show where to find more in-depth explanations. We will focus on the applications they have had in recent years and possible research opportunities.

In this section, ranging from Figures 3 to 10, statistical information is provided regarding several aspects. In Figure 3 it can be seen that the number of papers on volumetric imaging has increased in recent years, and from 2014 to 2016 no papers were published. Note that only Figure 3 includes all 72 papers, the non-volumetric application papers are not included in the

remaining diagrams. Magnetic resonance imaging (MRI) and computed tomography (CT) are the two most popular modalities, Figure 4, with more than half of the papers considered applied in the medical field, Figure 5.

The modalities used in the reviewed papers are: magnetic resonance imaging (MRI) [McRobbie et al. \[2017\]](#), CT [Scarfe et al. \[2006\]](#), positron emission tomography (PET) [Townsend \[2008\]](#), radiographs [Phillips \[1897\]](#), optical coherence tomography (OCT) [Bezerra et al. \[2009\]](#), microscopy¹ [Fadereo et al. \[2018\]](#), computer-aided design (CAD) [Shivegowda et al. \[2022\]](#), red, green, blue depth sensors (RGB-D) [Zhou et al. \[2021\]](#), seismic reflection data [Dumay and Fournier \[1988\]](#), focused ion beam scanning electron microscopy (FIB-SEM) [Fischer et al. \[2020\]](#), and kelvin probe force microscopy (KPFM) [Melitz et al. \[2011\]](#).

Reconstruction is the main application of GANs in the non-medical context and image translation in the medical context, as can be seen in Figure 6. It is worth noting that most papers in the field of medicine are related to humans, Figure 5. The most commonly studied organ in the medical field is the brain, as shown in Figure 7. This popularity results from the increasing use of MRI to study the brain and the need for pipelines to process these images and automate processes. MRI scans of the brain are also easier to process/analyze compared to the rest of the body because there is less movement and variation, resulting in fewer artefacts and faster acquisitions.

In Figure 8 it is possible to find the number of publications per year in relation to the different modalities. CT and MRI are present almost every year, which corresponds to the reality of volumetric data acquisition. Especially in the medical field, MRI and CT are widely used. In the non-medical field, CT and X-rays are mainly used, but CAD is also intensively studied due to development of sensors such as RGB-D [Zollhöfer et al. \[2018\]](#) and light detection and ranging (LiDAR)² [Collis \[1970\]](#).

Figures 9 and 10 contain the number of papers that use a particular loss function or evaluation metric. Most of them are easy to explain and widely known, but some require some context to be understood, so

¹What is Electron Microscopy? (accessed [06-06-2022])

²What is LiDAR? (accessed [06-06-2022])

it is necessary to access all the references given in **Sections 3.1** and **3.2** for better understanding.

Figure 9 shows that the WGAN/WGAN-GP (Wasserstein GAN / Wasserstein GAN with gradient penalty) is the most commonly used loss function due to its ability to stabilise and prevent vanishing gradient [Gulrajani et al. \[2017\]](#), followed by the mean absolute error (MAE) and cross-entropy (CE), which are commonly used to avoid some instability and mode collapse ([Thanh-Tung and Tran \[2020\]](#)), mainly in the first steps of training.

As can be seen in Figure 10, the peak signal-to-noise ratio (PSNR) is the most common evaluation metric as it is able to evaluate reconstructions, which can be considered one of the main applications of volumetric GANs, although GANs are explored for numerous other purposes. Structural similarity index measure (SSIM) is the second most used metric because it can better assess the quality of the data, taking into account human perception. Usually, Fréchet inception distance (FID) is considered the most reliable metric. However, it is not easy to adapt to volumetric data and even the existing adaptations are not well accepted by researchers. Accuracy is not really used to assess the quality of the images in terms of perception, but to assess the quality of the data to perform data augmentation, and to assess the improvements of other tasks when synthetic data are used, e.g. segmentation and classification tasks. For that reason, dice similarity coefficient (DSC), sensitivity and F1-score are also commonly used.

The proposed taxonomy for medical and non-medical GANs is shown in Figures 11 and 12. The taxonomy has been divided into two different figures due to its size. First, a distinction is made between medical and non-medical applications, then by application, architecture, and the respective papers. For example: A user wants to perform a modality translation of volumetric brain images, following "Medical" → "Image Translation" → "Brain" will find the architectures used and the corresponding papers; Another user wants to reconstruct non-medical 3D volumes from 2D images, following "Non-Medical" → "Reconstruction (2D to 3D)" will find all available architectures and papers for 2D to 3D reconstruction.

Figure 13 shows each different architecture used in each application for medical and non-medical purposes, showing that cGAN-based and CycleGAN-

based architectures are used for several different applications.

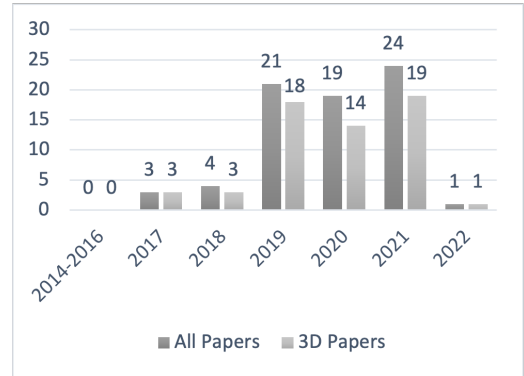


Figure 3: Number of papers per year.

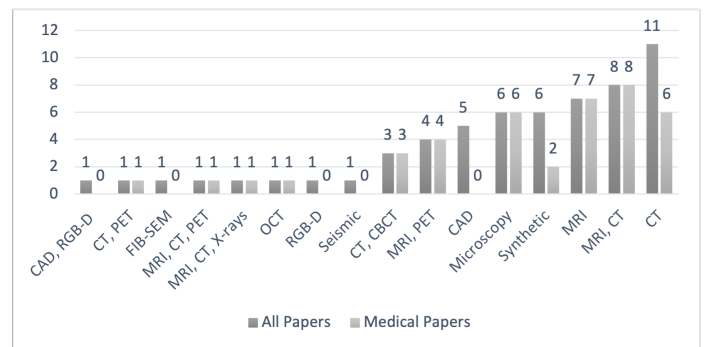


Figure 4: Number of volumetric data papers per modality.

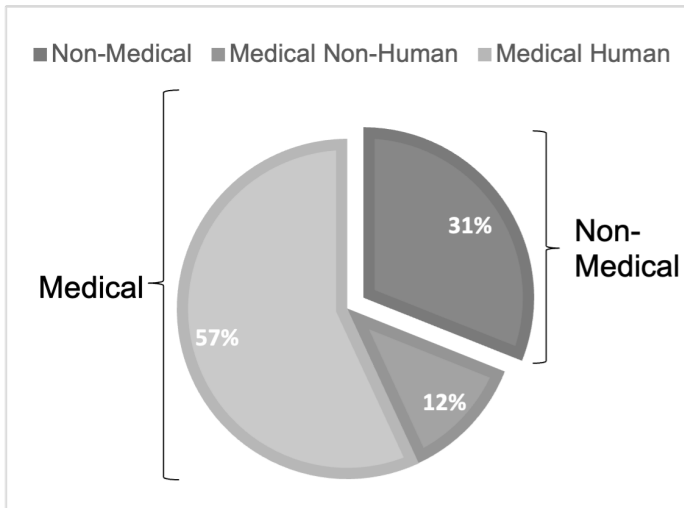


Figure 5: Number of papers on volumetric data with medical and non-medical application. The medical papers are divided into human and non-human applications.

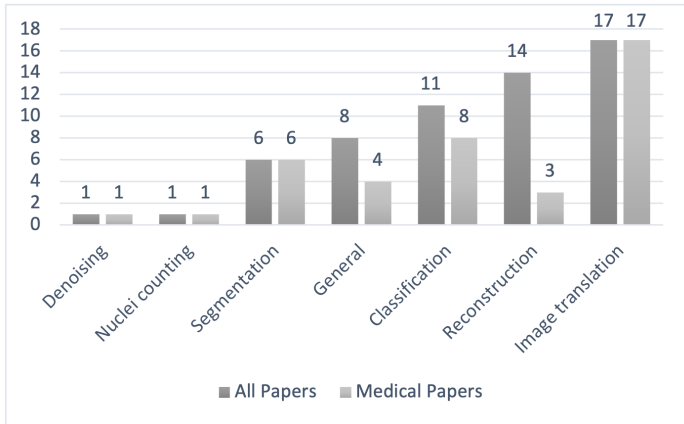


Figure 6: Number of volumetric data papers per non-medical application.

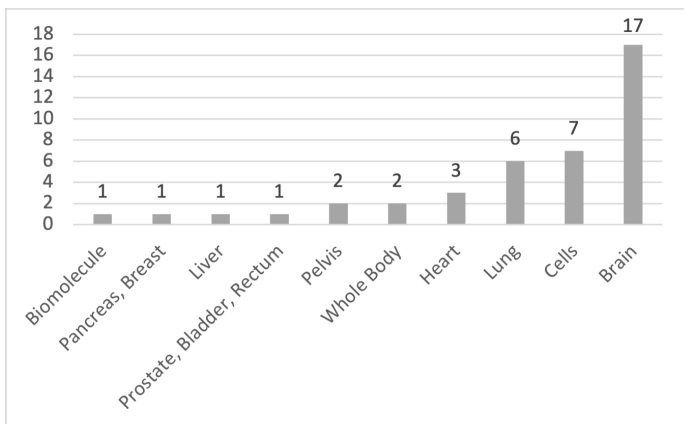


Figure 7: Number of medical papers per organ.

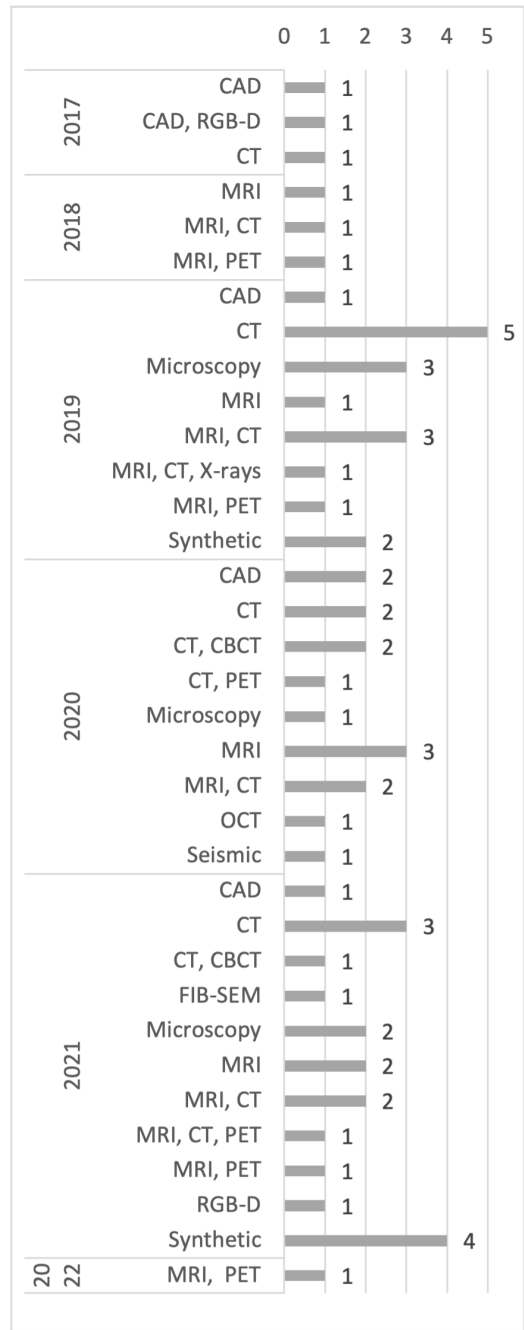


Figure 8: Number of papers per modality per year.

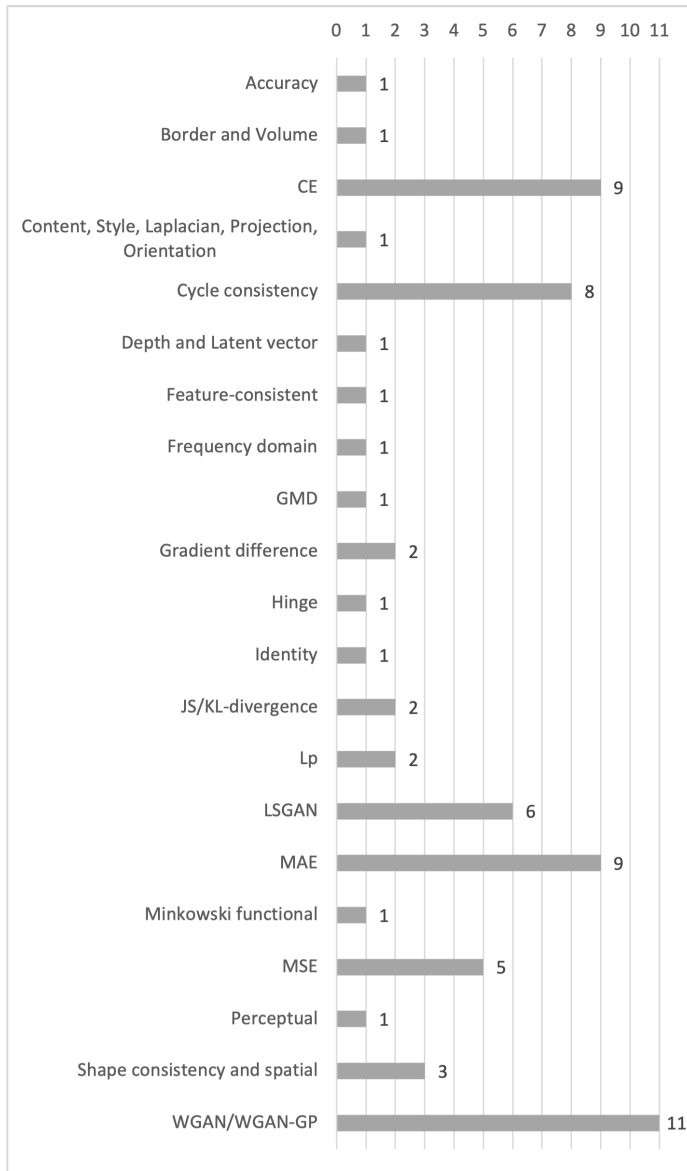


Figure 9: Number of papers per loss function/functions.

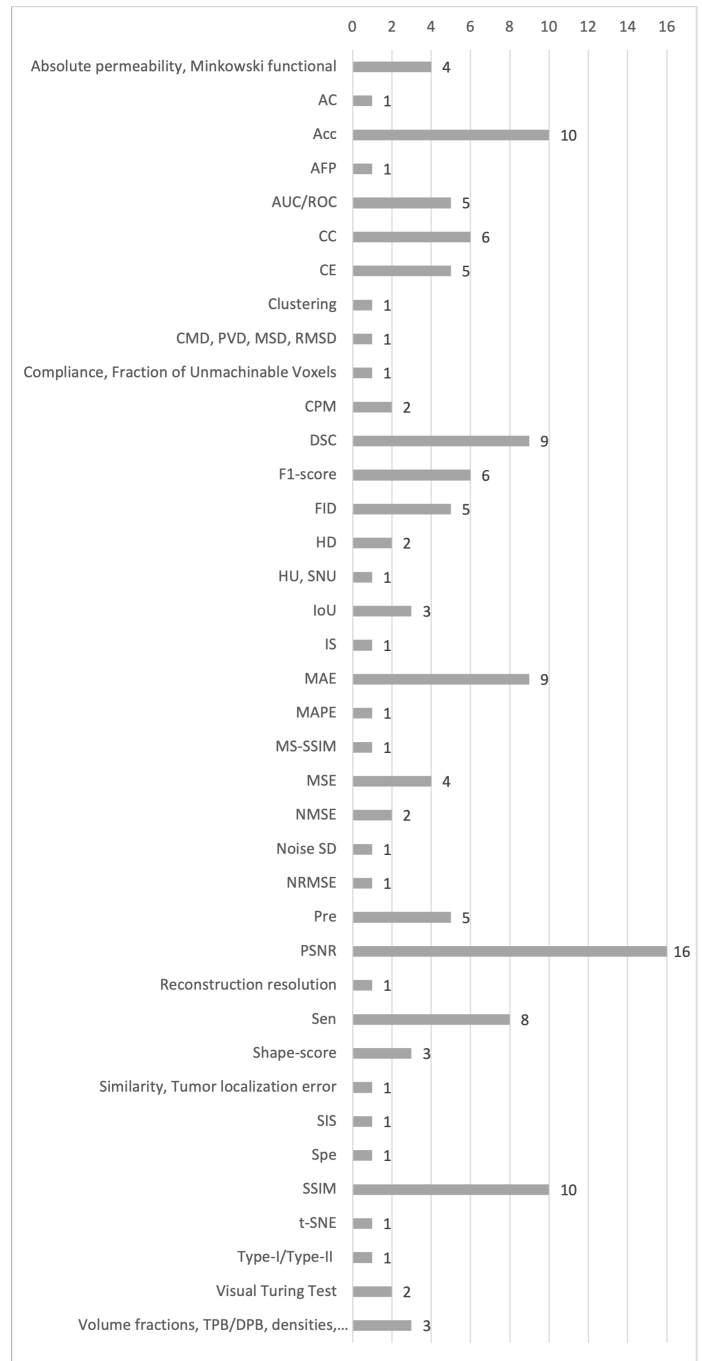


Figure 10: Number of papers per evaluation metric/metrics. The incomplete loss function description in the figure is "Volume fractions, triple phase boundary (TPB), double phase boundary (DPB), densities, relative surface area, relative diffusivity, surface area, two-point correlation function (TPCF)".

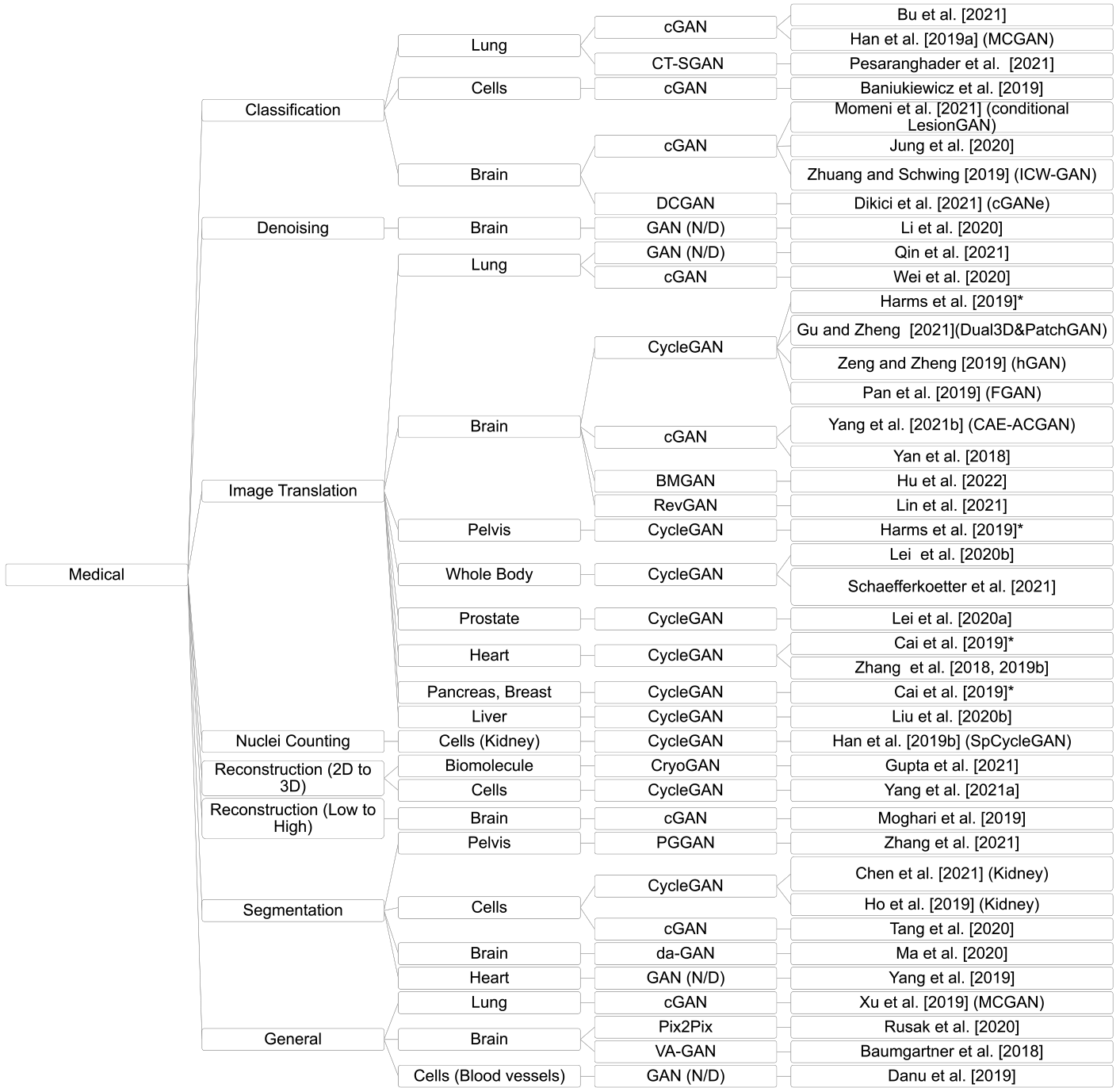


Figure 11: Proposed taxonomy of medical volumetric GANs. *These works performed tests in more than one structure.

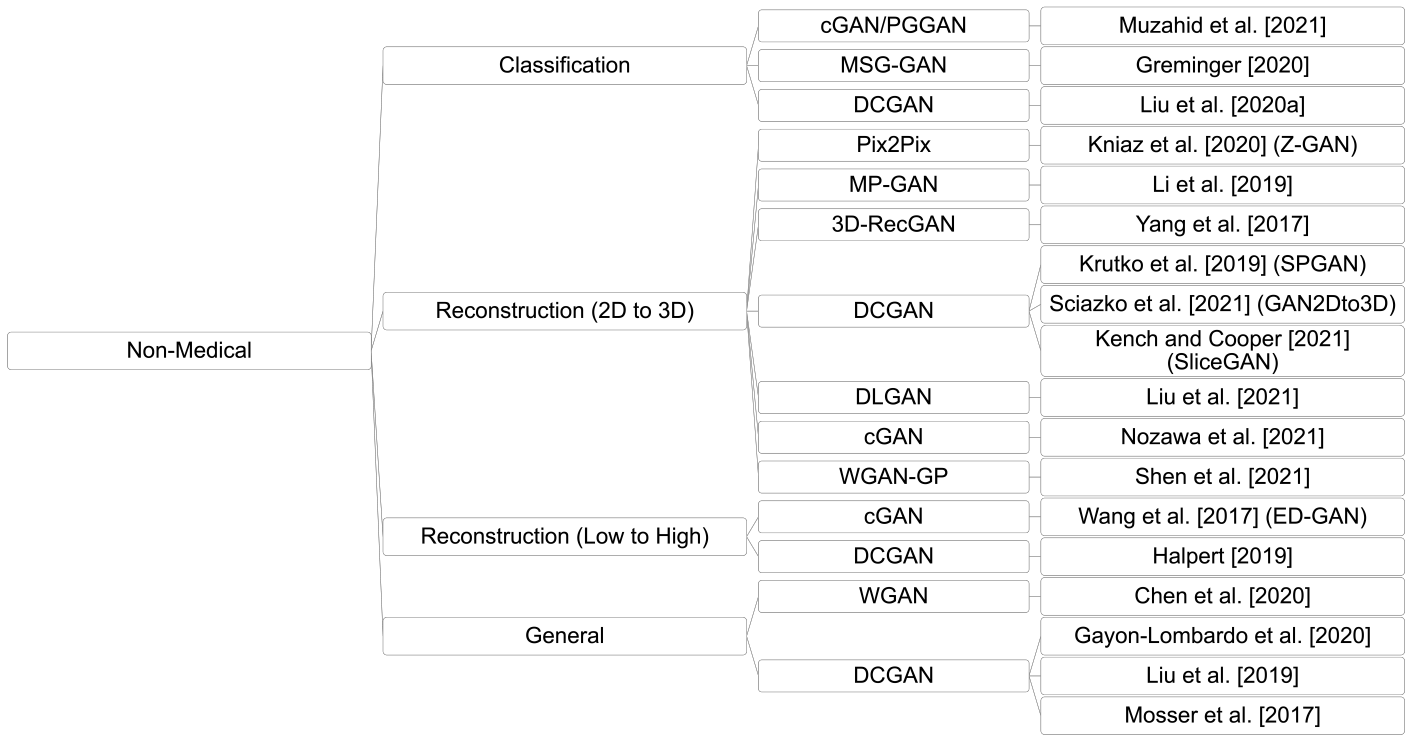


Figure 12: Proposed taxonomy of non-medical volumetric GANs.

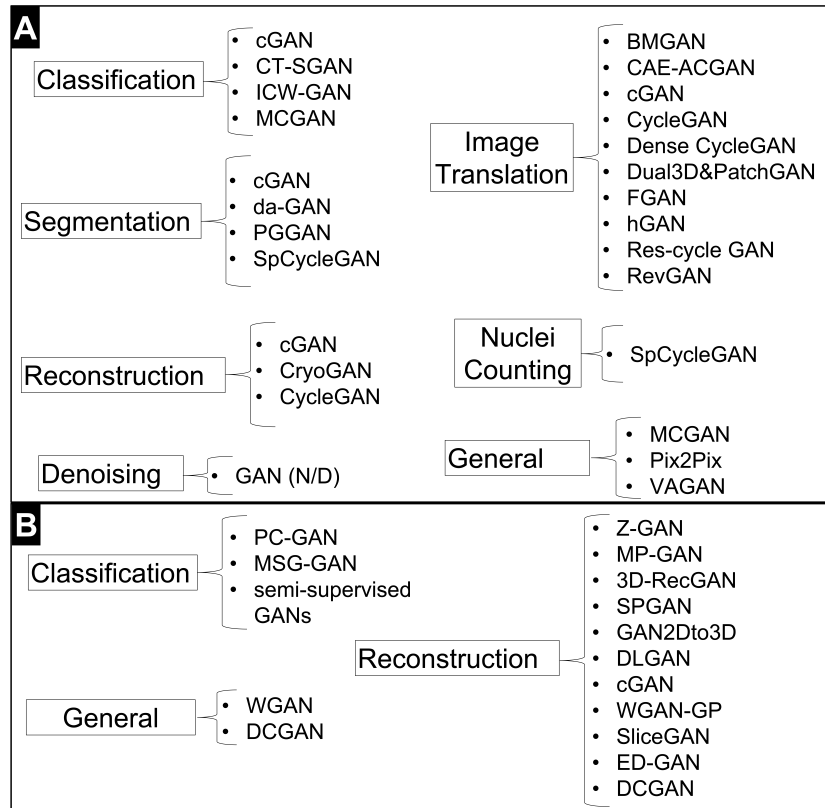


Figure 13: Architectures used in every A) medical application B) non-medical application.

3.1 Loss Functions

This section provides a brief explanation of each loss function used in the reviewed papers, along with any references needed and each paper in which each metric was used. It is important to note that some loss functions were developed for a specific problem and only make sense in that context, or they are an adaptation of existing metrics, such as shape consistency and identity. The loss functions are mainly ordered alphabetically, but some of them are very similar, therefore they are explained together.

Accuracy: Accuracy is defined as the number of correct predictions among all predictions. It was only used as a loss function in [Muzahid et al. \[2021\]](#), where the discriminator was trained not only to give the true value but also to give the correct classification of the objects.

Adversarial: From GANs' first paper [Goodfellow et al. \[2014\]](#), the adversarial loss is given by the discriminator's correct classification of the realism of the data received. If the discriminator gives a correct prediction, the generator is penalised; if it gives an incorrect one, the discriminator itself is penalised. This is also known as the "minmax game".

Cross Entropy (CE): CE, also referred to as reconstruction loss, is used to measure the difference between two distributions [Suh et al. \[2021\]](#); [Gecer et al. \[2020\]](#); [Zhang et al. \[2021\]](#); [Gayon-Lombardo et al. \[2020\]](#); [Dikici et al. \[2021\]](#); [Jung et al. \[2020\]](#); [Lei et al. \[2020b\]](#); [Wang et al. \[2017\]](#); [Liu et al. \[2020a\]](#); [Nozawa et al. \[2021\]](#). Binary Cross Entropy (BCE), also called sigmoid CE, is usually used to train a binary classifier [Ramos et al. \[2018\]](#); [Ruby and Yendapalli \[2020\]](#); [Olberg et al. \[2019\]](#). In this context, BCE measures the difference between the real and predicted distribution of the data. Higher values of BCE correspond to higher uncertainty of the discriminator, and therefore higher difference between distributions [Olberg et al. \[2019\]](#). The modified CE is used in [Yang et al. \[2017\]](#) to strongly penalise false positives compared to false negatives due to the properties of the data used.

Border and Volume: Implemented in [Momeni et al. \[2021\]](#), border and volume losses are used to im-

prove the quality of the MRI scans generated for their specific problem. Volume losses penalise the differences between the input volume (a numerical value) and the volume of the cerebral microbleed generated. Border losses force the edges of the generated scan to be 1.

Content, Style, Laplacian, Projection, Orientation:

All of these loss functions are used in [Shen et al. \[2021\]](#). The content and the style losses were based on [Gatys et al. \[2016\]](#) and are per-pixel comparisons focused on different levels of the convolution network. The Laplacian, the projection and the orientation losses, are also per-pixel comparisons and are explained with more detail in [Shen et al. \[2021\]](#).

Cycle consistency: Cycle consistency loss can be defined as: if G is the generator and G^{-1} is its inverse transformation, x is the input image and $G(x)$ is the output of the generator having x as input; then $G^{-1}(G(x)) \approx x$. It is used mainly for the CycleGAN [Zhu et al. \[2017\]](#) training, and widely used for image translation when no paired data are available. The comparison between the two images is made per-pixel using MAE as in the original paper, or other metrics such as mean squared error (MSE) or CE. It is used in [Bongini et al. \[2021\]](#); [Jung et al. \[2020\]](#); [Harms et al. \[2019\]](#); [Lei et al. \[2020a\]](#); [Schaefferkoetter et al. \[2021\]](#); [Lin et al. \[2021\]](#); [Chen et al. \[2021\]](#); [Han et al. \[2019b\]](#); [Yang et al. \[2021a\]](#).

Depth and Latent vector: The depth loss penalises the difference between the generated 3D voxel and the input 2.5D voxel grid. The latent vector minimises the distance between the latent vector from the input data and the target latent vector. Both loss functions are explained in [Liu et al. \[2021\]](#).

Feature-consistent: The feature-consistent loss is defined in [Pan et al. \[2019\]](#) and measures the difference between scans that share the same modality. This loss function is very similar to the cycle consistency loss.

Focal: Focal regression loss was used in [Bird et al. \[2021\]](#) to improve performance in hard-to-predict bone regions. It was introduced by [Lin et al. \[2017\]](#) to

reduce the side effect of class imbalance when training dense detectors. It is based on CE, with a tuning parameter introduced to increase the weight of high difficulty classes and avoid overloading the loss function when class imbalance exists. Automated focal loss was introduced by [Weber et al. \[2020\]](#) and proposes a strategy to automate the fine-tuning of the new hyperparameter, reducing this time-consuming task.

Frequency domain: Frequency domain loss was used by [Ma et al. \[2020\]](#) to reduce blurring. It is very similar to MAE loss but uses the Fast Fourier Transform to transfer the MAE comparison to the frequency domain.

Gradient Magnitude Distance (GMD): The GMD loss is used in [Harms et al. \[2019\]](#) and is very similar to the Gradient Difference Loss [Mathieu et al. \[2016\]](#), but adapted to volumetric data.

Gradient difference: Comparable to MAE or MSE loss, gradient difference loss is another metric for measuring the distance between two images/volumes that improves edge sharpness. A Sobel operator [Kanopoulos et al. \[1988\]](#) is used to measure the gradient difference between the generated image and the target image in the desired orientation, i.e. x , y or z . It was used in [Liu et al. \[2020b\]](#); [Ma et al. \[2020\]](#) with a better explanation in the latter.

Hinge: The hinge loss, as explained in [Rosasco et al. \[2004\]](#), is a loss function widely used for classification. In this case, it was used in [Greminger \[2020\]](#) to measure the distance between the output of the discriminator and the target output. In [Posilovic et al. \[2021\]](#) it was used to compare between the output of the generator and the target image.

Identity: The identity loss used in [Schaefferkoetter et al. \[2021\]](#), as explained in [Zhu et al. \[2017\]](#), uses the MAE distance to measure the distance between the input and the corresponding output of the generator and works as a cycle consistency loss helper in the CycleGAN architecture to avoid unnecessary changes in the intermediate step.

Jensen-Shannon (JS) and Kullback–Leibler divergence (KL-divergence): The JS loss is used in [Pesaranghader et al. \[2021\]](#). It is based on the KL-divergence to measure the distance between two probability distributions. The KL-divergence (also known as relative entropy) is used in [Posilovic et al. \[2021\]](#); [Amirrajab et al. \[2020\]](#); [Hu et al. \[2022\]](#). A more detailed explanation can be found in the first paper on GANs [Goodfellow et al. \[2014\]](#). The KL-divergence is also used in [Hu et al. \[2022\]](#) to reduce the distribution difference between the encoded vector and the sampled latent vector, and it is denominated by KL-divergence constraint.

L_p : The L_p is used in [Liu et al. \[2020b\]](#); [Harms et al. \[2019\]](#) with $p = 1.5$ to avoid the defects introduced by the MSE (L_2) and MAE (L_1) losses, specifically, the blurry images by MSE and the misclassification by MAE.

Least Squares (LSGAN): The LSGAN loss [Mao et al. \[2017\]](#) uses the least squares loss function instead of the sigmoid cross-entropy loss function to avoid vanishing gradients. It is used in the [Bongini et al. \[2021\]](#); [Slossberg et al. \[2019\]](#); [Han et al. \[2019a\]](#); [Xu et al. \[2019\]](#); [Cai et al. \[2019\]](#); [Hu et al. \[2022\]](#); [Yang et al. \[2021a\]](#) papers.

Mean Absolute Error (MAE or L_1): MAE [Sammut and Webb \[2010d\]](#) is often used in regression problems to compare the distance between two images/volumes, i.e. it is the absolute average difference between the predicted value and the expected value. It is used in several papers to stabilise GAN training, as is the MSE, however, using MAE can lead to more realistic images. This may be one reason why MAE is one of the most frequently used loss functions in the papers of this review.

Minkowski functional: The Minkowski functional is used in [Chen et al. \[2020\]](#) as a loss function to measure the distance between geometric features of the volumes, i.e. porosity, specific surface area, average width and Euler number. It is a precise technique for analysing geometric structures that can also be used for biomedical image analysis [Depeursinge et al.](#)

[2014]. Boehm et al. [2008] presents precise definitions of these measures.

Mean Squared Error (MSE or L_2): MSE Sammut and Webb [2010e], like MAE, is often used in regression problems and to compare two images/volumes. It is the average of the squared difference between the prediction and the ground truth. Using this metric as a loss function results in blurry images.

Perceptual: Perceptual loss uses a pre-trained deep convolutional neural network to measure the perceptual differences between two images. In the first publication Johnson et al. [2016], a VGG-16 network was used Simonyan and Zisserman [2014], pre-trained on the ImageNet dataset Russakovsky et al. [2015]. However, this concept can be extended to other pre-trained networks, such as VGG-19. This metric was used in one of the state-of-the-art publications on GANs Karras et al. [2019]. It was also used in Wang et al. [2021] (VGG-19) and Hu et al. [2022] (VGG-16).

Shape consistency and spatial: Directly related to cycle consistency loss in Zhang et al. [2019b, 2018]; Cai et al. [2019], shape consistency loss is used to ensure anatomical structure invariance through the use of segmentation networks, i.e. if a scan of a certain modality (e.g. MRI) has a certain semantic label, the generated scan of the other modality must have the same semantic label. It is similar to identity loss as it is used to regulate the intermediate step of CycleGAN training. Spatial loss Fu et al. [2018] is also related to cycle consistency loss in Chen et al. [2021]; Han et al. [2019b] and serves the same purpose, but uses a binary label instead of a semantic label to segment networks.

Wasserstein GAN (WGAN) and WGAN with Gradient Penalty (WGAN-GP): The WGAN-GP is an improvement over the original WGAN Arjovsky et al. [2017], which performs weight pruning to achieve 1-Lipschitz functions that can bring undesirable problems such as the vanishing of the gradient and the need for high attention to hyperparameters. Using WGAN-GP Gulrajani et al. [2017] makes it possible to achieve Lipschitz continuity with almost no hyperparameter tuning. The WGAN loss is used in Posilovic

et al. [2021]; Chen et al. [2020]; Li et al. [2020]; Kench and Cooper [2021]. The WGAN-GP loss is used in Suh et al. [2021]; Wang et al. [2021]; Gecer et al. [2020]; Slossberg et al. [2019]; Pesaranghader et al. [2021]; Han et al. [2019a]; Jung et al. [2020]; Zhuang and Schwing [2019]; Baumgartner et al. [2018]; Yang et al. [2017]; Gupta et al. [2021]; Shen et al. [2021].

3.2 Evaluation Metrics

This section presents a brief explanation of each evaluation metric used in the papers studied, along with the required references and each paper in which the particular metric was used. It is important to note that some metrics are only used for specific purposes and are not well-known, or are sometimes just an adaptation of existing metrics for the problem in question but with a different name, such as fraction of unmachinable voxels and shape-score. The metrics are mainly ordered alphabetically, but some of them are very similar, therefore they are explained together.

Absolute permeability, Minkowski functional: Absolute permeability is used in Krutko et al. [2019] to assess the quality of generated porous media volumes. It is usually used in conjunction with Minkowski functional. This metric is calculated using a pore network model. The Minkowski functional is already explained in the **Section 3.1**. It is used in Chen et al. [2020]; Krutko et al. [2019]; Mosser et al. [2017] for the evaluation step.

Attenuation Correction (AC): Attenuation in PET scans is caused by photons that are lost through absorption in the body, leading to artifacts. AC can be performed with MRI or CT scans as well as other techniques Chen and An [2017]. The use of synthetic CT scans to perform AC is performed in Schaefferkoetter et al. [2021] and evaluated in comparison to MRI-based correction.

Accuracy, Sensitivity, Specificity, Precision, Average False Positives (AFP), Type-I/Type-II errors: The metrics accuracy, sensitivity, specificity Baratloo et al. [2015], precision Ting [2010b] and AFP are often used in machine learning. To calculate these metrics, a confusion matrix Ting [2010a] is usually created. The metric used should be chosen carefully depending on

the problem, as high performance in one of the metrics does not necessarily mean a good model. Accuracy is measured in Gecer et al. [2020]; Ge et al. [2020]; Pesaranghader et al. [2021]; Jung et al. [2020]; Zhuang and Schwing [2019]; Wei et al. [2020]; Yan et al. [2018]; Muzahid et al. [2021]; Li et al. [2019]; Wang et al. [2017]; Chen et al. [2021]; Liu et al. [2020a]. Sensitivity, also known as recall, is measured in Ge et al. [2020]; Bu et al. [2021]; Momeni et al. [2021]; Zhuang and Schwing [2019]; Lei et al. [2020a]; Chen et al. [2021]; Ho et al. [2019]; Han et al. [2019b]; Baniukiewicz et al. [2019]. Specificity is measured in Ge et al. [2020]; Lei et al. [2020a]. Precision, also known as positive predictive value, is measured in Zhuang and Schwing [2019]; Chen et al. [2021]; Ho et al. [2019]; Han et al. [2019b]; Baniukiewicz et al. [2019]. The AFP metric is used in Dikici et al. [2021]. Type-I and Type-II errors, also known as false positive and false negative errors, are used in Chen et al. [2021]. It can be also be used as $1 - \text{Specificity}$ and $1 - \text{Sensitivity}$, respectively.

Area Under the Curve (AUC), Receiver Operating Characteristic curve (ROC): AUC Sammut and Webb [2010a] is the area under the ROC curve Flach [2010] and is intrinsically related to sensitivity and false positive rate ($1 - \text{Specificity}$). The AUC is used in Mokhayeri et al. [2020]; Baek et al. [2020]; Momeni et al. [2021]; Pan et al. [2019]; Yan et al. [2018]. The ROC curve is used in the aforementioned papers and in Momeni et al. [2021]. The AUC is used in Baek et al. [2020] to evaluate the results using the area under the curve of the ratio of Correct Keypoint (PCK).

Average Hausdorff Distance (HD) and surface HD: The average HD and surface HD are used in Amirrajab et al. [2020]; Zhang et al. [2021]; Lei et al. [2020a] to measure the distance between sets of pixels/voxels in ground truth and prediction Kazemifar et al. [2018]. A small value of HD corresponds to a small distance between each voxel in the prediction and a point in the ground truth.

Volume fractions, Triple Phase Boundary/Double Phase Boundary (TPB/DPB) densities, relative surface area, relative diffusivity, surface area, Two-Point Correlation Function (TPCF): All these metrics are used for microstructural characterisation.

The average volume fractions, volume fraction variations, and TPB/DPB densities are measurements used in Sciazko et al. [2021] to evaluate the quality of 3D fuel cell electrode microstructures. Volume fraction, relative surface area and relative diffusivity are measurements used in Kench and Cooper [2021] to evaluate the quality of various microstructures, including a battery cathode. The phase volume fraction, relative diffusivity, specific surface area, TPCF and TPB are used in Gayon-Lombardo et al. [2020] to measure the quality of electrode microstructures.

Correlation Coefficient (CC), Pearson CC (PCC), Normalised Cross Correlation (NCC): CC, PCC, and NCC Kirch [2008] are the linear association of two variables. They are used in Yang et al. [2021a]; Schaeferkoetter et al. [2021]; Bittner et al. [2018]; Baumgartner et al. [2018]; Harms et al. [2019]; Lei et al. [2020b]; Liu et al. [2020b] to assess the quality of the volumes generated.

Cross Entropy (CE): Already explained in Section 3.1. It was used during the assessment phase in Dikici et al. [2021]; Yang et al. [2017]; Wang et al. [2017]; Liu et al. [2021, 2020a].

Clustering: Clustering is used to divide a population of data points into a certain number of groups Sammut and Webb [2010b]. It was used in Muzahid et al. [2021] to check whether the class distribution of the generated samples could be easily split, i.e. whether the generator was able to learn the different classes.

Center of Mass Distance (CMD), Percentage Volume Difference (PVD), Mean Surface Distance (MSD), Residual Mean Square Distance (RMSD): CMD, PVD, MSD and RMSD are used in Lei et al. [2020a]. The CMD and PVD are used to measure the distance between the automatic and manual segmentation contours' center distance and volume differences and the MSD and RMSD are used to measure the surface distances of the two contours. The CMD, MSD, and RMSD are measured in millimetres.

Compliance, Fraction of Unmachinable Voxels: The compliance and fraction of unmachinable vox-

els are used in [Greminger \[2020\]](#) to measure the difference between machinable designs generated by GANs versus the traditional topology optimisation algorithm.

Competition Performance Metric (CPM): The CPM score used in [Bu et al. \[2021\]](#); [Han et al. \[2019a\]](#) is the average sensitivity at seven predefined false positive rates: 1/8, 1/4, 1/2, 1, 2, 4 and 8 FPs / scan according to the lung nodule analysis (LUNA16) challenge [Setio et al. \[2017\]](#).

Dice Similarity Coefficient (DSC), F1-score: DSC [Taha and Hanbury \[2015\]](#) and F1-score [Sammut and Webb \[2010c\]](#) are two similar metrics when applied to Boolean data, but they have different applications. DSC is also known as the overlap index and is the most commonly used metric for evaluating segmentation in volumetric medical imaging. The F1-score is used when the focus is on maximising both precision and recall. The F1-score is used in [Chen et al. \[2021\]](#); [Ho et al. \[2019\]](#); [Han et al. \[2019b\]](#); [Baniukiewicz et al. \[2019\]](#); [Liu et al. \[2020a\]](#). The macro F1-score (variation of F1-score) is used in [Zhuang and Schwing \[2019\]](#). The DSC is used in [Amirrajab et al. \[2020\]](#); [Zhang et al. \[2021\]](#); [Rusak et al. \[2020\]](#); [Ma et al. \[2020\]](#); [Li et al. \[2020\]](#); [Lei et al. \[2020a\]](#); [Zhang et al. \[2019b, 2018\]](#); [Cai et al. \[2019\]](#); [Chen et al. \[2021\]](#)

Fréchet Inception Distance (FID), Inception Score (IS): FID compares the distribution of generated images with real images. [Heusel et al. \[2017\]](#) claims that this metric can capture the similarity between generated images and real images better than IS and is consequently the most commonly used metric to assess the quality of GANs. However, it is not widely used for volumetric assessment. Usually the volumes are sliced in all three axes to allow the use of the FID, but this practice is not well accepted and therefore not widely used. The IS [Salimans et al. \[2016\]](#) uses an inception pre-trained model to classify the generated images and is used in [Pesaranghader et al. \[2021\]](#). The FID is used in [Mokhayeri et al. \[2020\]](#); [Pesaranghader et al. \[2021\]](#); [Dikici et al. \[2021\]](#); [Jung et al. \[2020\]](#); [Hu et al. \[2022\]](#); [Li et al. \[2019\]](#).

Hounsfield Unit (HU), Spatial Non-Uniformity (SNU): HU [Kamalian et al. \[2016\]](#) is a relative scale to measure the attenuation of the X-ray beam in a given voxel. This value is particularly important in the CT reconstruction phase. It is used in [Bird et al. \[2021\]](#); [Liu et al. \[2020b\]](#). The SNU is nothing more than the difference of HU in the same material, used in [Harms et al. \[2019\]](#).

Intersection-over-Union (IoU): The IoU or Jaccard index [Taha and Hanbury \[2015\]](#) is used in [Kniaz et al. \[2020\]](#); [Yang et al. \[2017\]](#); [Liu et al. \[2021\]](#) to measure the intersection of two distributions over the union of the two distributions.

MAE, Relative Mean Absolute Difference (RMAD), Normalized Median Absolute Deviation (NMAD), Mean Absolute Percentage Error (MAPE): The MAE is already explained in the [Section 3.1](#). MAE is used in [Bird et al. \[2021\]](#); [Lei et al. \[2020b\]](#); [Bittner et al. \[2018\]](#); [Rusak et al. \[2020\]](#); [Qin et al. \[2021\]](#); [Harms et al. \[2019\]](#); [Yang et al. \[2021b\]](#); [Liu et al. \[2020b\]](#); [Zeng and Zheng \[2019\]](#); [Hu et al. \[2022\]](#); [Pan et al. \[2019\]](#) for the assessment step. The RMAD is the MAE divided by the arithmetic mean used in [Gorbatsevich et al. \[2019\]](#). The NMAD is used and explained in [Bittner et al. \[2018\]](#). The MAPE is explained in [De Myttenaere et al. \[2016\]](#) and used in [Han et al. \[2019b\]](#). It is similar with the aforementioned MAE metrics, however it can lead to different results, since MAPE is biased by the negative errors.

MSE, Root MSE (RMSE), Normalised MSE (NMSE), Normalised Root MSE (NRMSE): The MSE is already explained in [Section 3.1](#). The MSE is used in [Slossberg et al. \[2019\]](#); [Rusak et al. \[2020\]](#); [Yang et al. \[2019\]](#); [Schaefferkoetter et al. \[2021\]](#); [Shen et al. \[2021\]](#) for the assessment step. The RMSE is the root version of the MSE used in [Olberg et al. \[2019\]](#); [Bittner et al. \[2018\]](#). The NMSE is a normalised version of the MSE with respect to the signal intensity used in [Moghari et al. \[2019\]](#); [Lei et al. \[2020b\]](#). The NRMSE is a normalised version of the RMSE used in [Yang et al. \[2021a\]](#).

mean Average Precision (mAP): mAP is used in [Bongini et al. \[2021\]](#); [Mokhayeri et al. \[2020\]](#) to eval-

uate object detection models. However, this metric was only used in the non-3D works mentioned in this review.

Noise SD: The noise SD is used in [Li et al. \[2020\]](#) to measure the background noise levels to compare between methodologies of denoising.

Planning Target Volume (PTV): The PTV in radiotherapy incorporates the gross target volume (macroscopic extent of the tumor)/ clinical target volume, plus margins due to uncertainties of patient setup and beam adjustment. Organs at risk (OAR) are the critical structures in the vicinity of the target volume. The use of synthetic data to calculate the OAR [Grosu et al. \[2006\]](#) dose is assessed in [Bird et al. \[2021\]](#); [Olberg et al. \[2019\]](#).

Reconstruction resolution: The reconstruction resolution is used to assess the quality of reconstruction of single particles from noisy projections in [Gupta et al. \[2021\]](#).

Shape-score: The S-score is used in [Zhang et al. \[2019b, 2018\]](#); [Cai et al. \[2019\]](#) to evaluate the shape quality of the generated scans, i.e., less geometric distortions. This measures the difference between the input and the respective reconstruction.

Similarity, Tumor localization error: The similarity and tumor localization error are used in [Wei et al. \[2020\]](#) to assess the reconstruction quality.

Semantic Interpretability Score (SIS): The SIS introduced by [Seitzer et al. \[2018\]](#) to evaluate reconstruction performance was used in [Ma et al. \[2020\]](#). It uses a pre-trained segmentation model to segment the reconstructed images and measure the overlap between the new segmentation and the ground truth segmentation. [Seitzer et al. \[2018\]](#) claims that with this metric it is possible to evaluate models with more human perception than with SSIM or PSNR.

Signal-to-Noise Ratio (SNR), Peak SNR (PSNR): SNR measures the proportion of the desired signal relative to the background noise, expressed in decibels (dB). It is used in [Wang et al. \[2021\]](#). The PSNR

is usually used more to measure the quality of images/volumes, which is why it is more commonly used in medical imaging. It is used in [Olberg et al. \[2019\]](#); [Moghari et al. \[2019\]](#); [Rusak et al. \[2020\]](#); [Ma et al. \[2020\]](#); [Li et al. \[2020\]](#); [Harms et al. \[2019\]](#); [Lei et al. \[2020b\]](#); [Gu and Zheng \[2021\]](#); [Yang et al. \[2021b\]](#); [Liu et al. \[2020b\]](#); [Yang et al. \[2019\]](#); [Zeng and Zheng \[2019\]](#); [Hu et al. \[2022\]](#); [Lin et al. \[2021\]](#); [Pan et al. \[2019\]](#); [Tang et al. \[2020\]](#); [Yang et al. \[2021a\]](#). This metric is often used to assess the quality of enhanced images or reconstructions. A more detailed description can be found in [Nadipally \[2019\]](#).

Structural Similarity Index (SSIM), Multi-Scale Structural Similarity Index Measure (MS-SSIM): The SSIM [Wang et al. \[2004\]](#) extracts structural information from images, just like human visual perception. It is used in [Suh et al. \[2021\]](#); [Olberg et al. \[2019\]](#); [Moghari et al. \[2019\]](#); [Rusak et al. \[2020\]](#); [Ma et al. \[2020\]](#); [Gu and Zheng \[2021\]](#); [Yang et al. \[2021b\]](#); [Lin et al. \[2021\]](#); [Pan et al. \[2019\]](#); [Yan et al. \[2018\]](#); [Tang et al. \[2020\]](#); [Yang et al. \[2021a\]](#). MS-SSIM [Wang et al. \[2003\]](#) is based on SSIM, where filters are used to extend it for multi-scale measurements. It is used in [Hu et al. \[2022\]](#). These metrics are widely used in reconstruction problems.

Sliced Wasserstein Distance (SWD): SWD [Rabin et al. \[2011\]](#) is used in [Slossberg et al. \[2019\]](#) to measure similarities between images using an approximation of earth-movers distance.

t-Distributed Stochastic Neighbor Embedding (t-SNE): The t-SNE explained in [Van der Maaten and Hinton \[2008\]](#) is used in [Han et al. \[2019a\]](#) to visualise high-dimensional data distributions. It is a relevant technique to visualise whether the distribution of the generated data follows the real data distribution.

Visual: Visual assessment is the most commonly used evaluation to obtain a human perception of the images/scans produced. So far, there is no metric that can truly replace human perception, even though some metrics like FID or SSIM try to do so. Usually, researchers perform a visual review when training the

generative models. However, there are more sophisticated visual assessments, such as the visual turing test used in [Suh et al. \[2021\]](#); [Bu et al. \[2021\]](#); [Han et al. \[2019a\]](#), where experts are asked to assess the realism of the generated data. For example, visualisation of the height and strength distribution in [Wang et al. \[2021\]](#) is used to evaluate the quality of the images produced instead of using other metrics.

3.3 Non-3D data generation

Although not the main objective of this review, it is important to note that the main state-of-the-art papers of GANs use 2D images rather than volumes, e.g. [Karras et al. \[2018\]](#), [Brock et al. \[2019\]](#), [Isola et al. \[2017\]](#), and [Salimans et al. \[2016\]](#). Usually the initial techniques used in GANs are first developed using 2D and then adapted to volumes, e.g. using an adaptation of CycleGAN [Zhu et al. \[2017\]](#) to perform modality translation on volumes. FID, one of the most important metrics for assessing GANs, widely accepted and used by the community, was developed to be applied to 2D data. Some adaptations of this metric to volumes assessment are made, but are not equally accepted by the community.

Table 1 provides a summary of the work that is considered relevant but for which no volumetric data was generated. The list of abbreviations used in this table is the following:

List 1: List of abbreviations of Table 1:

- ACDC — Automated Cardiac Diagnosis Challenge;
- AgeDB — Age DataBase;
- ASPP — Atrous Spatial Pyramid Pooling;
- CFP — Celebrities in Frontal Profile;
- C-GAN — Controllable GAN;
- CityGML — City Geography Markup Language;
- CMR — Cardiac Magnetic Resonance;
- DSM — Digital Surface Model;
- mAP — mean Average Precision;
- NMAD — Normalized Median Absolute Deviation;
- Pixel/PC — Pixel from Point Cloud;
- RMAD — Relative Mean Absolute Difference;
- RMSE — Root Mean Square Error;
- SAR — Synthetic Aperture Radar;
- SCD — Sunnybrook Cardiac Data;
- SNR — Signal-to-Noise Ratio;
- SQ-AGGAN — SeQuential lung nodule synthesis using Attribute-Guided GAN;
- SWD — Sliced Wasserstein Distance;
- TBGAN — Trunk-branch based GAN;
- TCGA — The Cancer Genome Atlas;

Table 1: Compact overview of reviewed non-3D data studies, sorted by year of publication, indicating the modality, and the datasets used with the respective localisation, if available. It also shows the network used, the loss functions, the evaluation metrics and the resolution of the synthetic data generated. The abbreviations used in this table can be found in List 1 or in Section 1.1 (Acronyms and Abbreviations)

Study	Modality	Dataset	Network (G/D)	Loss function	Metrics	Comments
Suh et al. [2021]	CT	LIDC-IDRI ³	SQ-AGGAN	WGAN-GP, CE, MSE, MAE	VTT, SSIM	64×64
Bongini et al. [2021]	Thermal/RGB images and synthetic 3D models	Flir ⁴ and Unity engine ⁵	LSGAN	Adv, Cycle consistency	mAP	640×512
Posilovic et al. [2021]	Ultrasonic scan	9188 images (6 steel blocks)	SPADE GAN based ⁶	WGAN, MAE, KL-divergence, Hinge, MSE	Visual	256×256
Bird et al. [2021]	MRI, CT	90 anorectal patients, paired MRI/CT	cGAN	Adv, Focal ⁷ , MAE	MAE, PTV dose, HU	N/D (2D slices as input)
Wang et al. [2021]	SAR tomography	YunCheng airborne, TerraSAR-X in Barcelona	cGAN	WGAN-GP, Perceptual (VGG-19 ⁸)	Visual, SNR	1200×256
Mokhayeri et al. [2020]	RGB Images and 3D models	Chokepoint ⁹ , COX-S2V ¹⁰	C-GAN	Adv, MSE	FID, AUC, mAP	800×600
Baek et al. [2020]	RGB images	Dexter-object ¹¹ , Ego-Dexter ¹² , Hand Object-3D ¹³	GAN (N/D)	Adv, MAE	AUC	256×256

³LIDC-IDRI

⁴FLIR

⁵Unity engine

⁶SPADE

⁷Focal loss

⁸VGG network

⁹Chokepoint dataset

¹⁰COX-S2V

¹¹Dexter-object

¹²Ego-Dexter

¹³Hand Object-3D

Gecer et al. [2020]	3dMD scanner ¹⁴	MeIn3D ¹⁵ (and their own similar but not available), CFP ¹⁶ , AgeDB Database ¹⁷	TBGAN (PG-GAN+cGAN)	WGAN-GP, CE	Visual, Acc	112×112 (3D rendering by Marmoset Toolbag ¹⁸)
Amirrajab et al. [2020]	MRI	66 synthetic MRXCAT ¹⁹ , ACDC ²⁰ , SCD ²¹ , York Cardiac MRI ²² , 156 internal clinical CMR	XCAT-GAN	Adv, KL-divergence	Visual, DSC, HD	256×256
Ge et al. [2020]	MRI	TCGA ²³ , MICCAI BraTS 2017 ²⁴	Pairwise GAN ²⁵	Adv, MAE	Acc, Sen, Spe	N/D
Olberg et al. [2019]	MRI, CT	500, 1000, 1500, 2000, and 2400 paired CT/MRI	N/D, 2 Generators (U-Net, ASPP)	Sigmoid CE, MAE	RMSE, SSIM, PSNR, PTV dose	512×512
Gorbatsevich et al. [2019]	Synthetic	Terrain Generator ²⁶ (3 layers 1024×1024)	cGAN (U-net/ Patch-GAN)	Adv, MAE	RMAD	256×256
Slossberg et al. [2019]	3dMD scanner	5000 scans mapped to 2D (RGB images)	PGGAN	Adv (WGAN-GP or LSGAN)	SWD, MSE	1024×1024
Bittner et al. [2018]	LiDAR, DSM	CityGML data (Berlin 3D ²⁷ , Worldview-1, Worldview-2)	cGAN	Adv, MAE	MAE, NCC, RMSE, NMAD	256×256, Pixel/PC

¹⁴3dMD scanner

¹⁵MeIn3D

¹⁶CFP

¹⁷AgeDB

¹⁸Marmoset Toolbag

¹⁹MRXCAT

²⁰ACDC

²¹SCD

²²York Cardiac MRI

²³TCGA

²⁴MICCAI BraTS 2017

²⁵Pairwise GAN

²⁶World Machine

²⁷Berlin 3D

3.4 3D data generation

In this section is possible to find all volumetric papers in Tables 2, 3 and 4. Table 2 contain all papers where CT or MRI scans are used, sorted by modality and then by year. If a dataset has no link, this means that it is not available or has not been found. The footnotes of the studies are the links to the available code/framework.

List 2: List of abbreviations of Table 2:

- AFP — Average False Positives;
- AIBL — Australian Imaging Biomarkers and Lifestyle;
- C3D — Convolutional 3D;
- CBF — Cerebral Blood Flows;
- cGANe — constrained GAN ensembles;
- CPM — Competition Performance Metric;
- CTP — CT Perfusion;
- CT-SGAN — CT Synthesis GAN;
- da-GAN — difficulty-aware attention GAN;
- IBC — Individual Brain Charting;
- ICW-GAN — Improved Conditional Wasserstein GAN;
- IS — Inception Score;
- JS — Jensen-Shannon loss;
- Li-ion battery — Lithium-ion battery;
- MCGAN — Multi-Conditional GAN;
- micro-CT — micro Computed-Tomography;
- LUNA — LUng Nodule Analysis;
- NLST — National Lung Screening Trial;
- Noise SD — background noise levels;
- OCT — Optical Coherence Tomography;
- ODT — Optical coherence Doppler Tomography;
- ROC — Receiver Operating Characteristic curve;
- SIS — Semantic Interpretability Score;
- SOFC — Solid Oxide Fuel Cell;
- SPGAN — Slice to Pores GAN;
- SSA — Specific Surface Area;
- TPCF — Two-Point Correlation Function;
- t-SNE — t-distributed Stochastic Neighbor Embedding;
- VA-GAN — Visual Attribution GAN;
- XCT — X-ray Computed Tomography;

Table 3 presents a summary of all multimodal papers where CT, MRI, PET and/or CBCT were used. The papers Zhang et al. [2019b, 2018]; Cai et al. [2019] are interconnected and should therefore be read together for better understanding.

List 3: List of abbreviations of Table 3:

- AC — Attenuation Correction;
- BMGAN — Bidirectional Mapping GAN;

- CAE-ACGAN — Conditional Auto-Encoding, Auxiliary Classifier GAN;
- CMD — Center of Mass Distance;
- GMD — Gradient Magnitude Distance;
- FGAN — Feature-consistent GAN;
- hGAN — hybrid GAN (3D Generator and 2D Discriminator);
- MSD — Mean Surface Distance;
- MS-SSIM — Multi-Scale Structural Similarity Index Measure;
- PCC — Pearson Correlation Coefficient;
- PVD — Percentage Volume Difference;
- res-cycle GAN — residual block cycle-consistent GAN;
- RevGAN — Reversible GAN;
- RMSD — Residual Mean Square Distance;
- SNU — Spatial Non-Uniformity;
- S-score — Shape-score;

Table 4 contains the papers on the other modalities, such as CAD, RGB-D, FIB-SEM, microscopy, seismic and synthetic. The papers Ho et al. [2019]; Han et al. [2019b]; Chen et al. [2021] have some authors in common and complement each other.

List 4: List of abbreviations of Table 4:

- CC — Correlation Coefficient;
- cryo-EM — cryo-Electron Microscopy;
- diSPIM — dual inverted Selective Plane Illumination Microscope;
- DLGAN — Depth-preserving Latent GAN;
- DPB — Double Phase Boundary;
- FIB — Focused Ion Beam;
- KPFM — Kelvin Probe Force Microscopy;
- LSFM — Light Sheet fluorescence Microscopy;
- MAPE — Mean Absolute Percentage Error;
- MP-GAN — Multi-Projection GAN;
- MSG-GAN — Multi-Scale Gradient GAN;
- NRMSE — Normalized Root Mean Square Error;
- PC-GAN — Progressive Conditional GAN;
- PSF — Point Spread Functions;
- RecGAN — Reconstruction GAN;
- SpCycleGAN — Spatially Constrained CycleGAN;
- TPB — Triple Phase Boundary;
- Voxel/ PC — Voxelized point clouds;

Table 2: Compact overview of reviewed studies with modalities CT and MRI, sorted by modality and then by year of publication, indicating the modality, and the datasets used with the respective localisation, if available. It also shows the network used, the loss functions, the evaluation metrics, the resolution of the synthetic data generated, and whether or not it is a medical application. The abbreviations used in this table can be found in List 2 or in Section 1.1 (Acronyms and Abbreviations)

Study	Modality	Med	Dataset	Network (G/D)	Loss function	Metrics	Comments
Bu et al. [2021]	CT	Yes	LUNA16 ²⁸	cGAN (3D-Unet / 3D CNN)	Adv	VTT, Sen, CPM	32×32×32
Pesaranghader et al. [2021]	CT	Yes	NLST ²⁹ , LIDC ³⁰	CT-SGAN	WGAN-GP, JS	Visual, FID, IS, Acc	> = 224×224×224 (stacks 224×224×3)
Zhang et al. [2021]	CT	Yes	120 intact prostate cancer patients	PGGAN	Adv, CE	DSC, Average HD, Average Surface HD	64×128×128
Chen et al. [2020]	CT	No	Berea Sandstone ct scan	WGAN with two discriminators	WGAN, Minkowski functional	Minkowski functional	64×64×64
Gayon-Lombardo et al. [2020] ³¹	CT (XCT)	No	Li-ion battery cathode ³² , SOFC anode ³³	DCGAN	Adv, CE	Phase volume fraction, SSA, TPB, TPCE, Relative diffusivity	64×64×64
Liu et al. [2019]	CT	No	Berea sandstone ³⁴ , Estailades carbonate ³⁵	DCGAN	Adv	Visual	64×64×64, 128×128×1283
Krutko et al. [2019]	CT	No	Sandstone ³⁶	SPGAN (3D DCGAN based)	Adv	Minkowski functional, Absolute permeability	64×64×64
Moghari et al. [2019]	CT (CTP)	Yes	18 acute stroke patients	cGAN	Adv (N/D)	PSNR, NMSE, SSIM	64×64×64
Han et al. [2019a]	CT	Yes	LIDC ²⁸	MCGAN (UNET/Pix2Pix)	LSGAN, WGAN-GP	VTT, t-SNE, CPM	32×32×32
Xu et al. [2019]	CT	Yes	LIDC ²⁸	MCGAN	LSGAN, MAE, MSE	Visual	64×64×64

²⁸LUNA16

²⁹NLST

³⁰LIDC

³¹Pores for thought

³²Li-ion battery cathode

³³SOFC anode

³⁴Berea sandstone

³⁵Estailades carbonate (wrong in the paper)

³⁶Low-permeable sandstone sample from a hydrocarbon reservoir located in Russia rotationally scanned with an X-ray v|tome|x L240 GE system

Mosser et al. [2017] ³⁷	Micro-CT	No	Spherical Bead pack, Berea sandstone, oolitic, Ketton limestone ³⁸	DCGAN	Adv	Minkowski functional	64×64×64
Dikici et al. [2021]	MRI	Yes	217 post-gadolinium T1-weighted	cGANe (DC-GAN based)	CE	AFP, FID	16×16×16
Momeni et al. [2021]	MRI	Yes	AIBL ³⁹ , MICCAI Valdo 2021 ⁴⁰	conditional LesionGAN (cGAN based)	Adv, Volume, Border	AUC, Sen, ROC	11×11×11
Rusak et al. [2020]	MRI	Yes	ADNI ⁴¹	GAN (Pix2Pix based)	Adv, MAE	PSNR, SSIM, MAE, MSE, DSC	181×218×181
Jung et al. [2020]	MRI	Yes	ADNI ³⁹	CycleGAN (cGAN based)	WGAN-GP, CE, Cycle consistency	FID, Acc	192×192×(3,6,8) stacks 192×192×1
Ma et al. [2020]	MRI	Yes	Kulaga-Yoskovitz ⁴²	da-GAN	Adv, Gradient Difference, Frequency domain, MAE	Visual, PSNR, SSIM, SIS, DSC	384×512×384 (stacking 512 imgs of 384×384)
Zhuang and Schwing [2019]	MRI	Yes	OpenfMRI ⁴³ , IBC ⁴⁴	ICW-GAN	Adv, WGAN-GP	Acc, Macro F1, Pre, Sen	53×63×46
Baumgartner et al. [2018] ⁴⁵	MRI	Yes	ADNI ³⁹	VA-GAN (WGAN based 3D U-Net / C3D)	WGAN-GP, MAE	Visual, NCC	128×160×112
Li et al. [2020]	OCT	Yes	3D ODT of mouse CBF	GAN (N/D)	Adv, WGAN, MAE	PSNR, DSC, Noise SD	64×64, 64×64×64

³⁷PorousMediaGAN

³⁸Micro-CT Images and Networks

³⁹AIBL

⁴⁰MICCAI Valdo 2021

⁴¹ADNI

⁴²Kulaga-Yoskovitz

⁴³OpenfMRI

⁴⁴IBC

⁴⁵VA-GAN

Table 3: Compact overview of reviewed studies with multimodalities CT, MRI, PET and/or CBCT, sorted by modality and then by year of publication, indicating the modality, and the datasets used with the respective localisation, if available. It also shows the network used, the loss functions, the evaluation metrics, the resolution of the synthetic data generated. All studies are medical applications. The abbreviations used in this table can be found in List 3 or in Section 1.1 (Acronyms and Abbreviations)

Study	Modality	Dataset	Network (G/D)	Loss function	Metrics	Comments
Qin et al. [2021]	CT, CBCT	27 advanced lung cancer	GAN (Residual-Unet/CNN)	N/D	MAE	N/D
Wei et al. [2020]	CT, CBCT	4D-CT and raw CBCT projections	cGAN	Adv, MAE	Acc, Similarity, Tumor localization error	128×128×32
Harms et al. [2019]	CT, CBCT	24 brain and 20 pelvic CT/CBCT	res-cycle GAN	Adv, Cycle consistency, L1.5, GMD	MAE, PSNR, NCC, SNU	96×96×5 (stacked to produce 3D)
Lei et al. [2020b]	CT, PET	16 CT/PET	CycleGAN	Adv, MSE, CE	Visual, MAE, NMSE, NCC, PSNR	64×64×64
Gu and Zheng [2021]	MRI, CT	BrainWeb ⁴⁶	Dual3D& PatchGAN (3DGAN)	Adv	SSIM and PSNR	N/D
Yang et al. [2021b]	MRI, CT	9 healthy MRI ⁴⁷	CAE-ACGAN	Adv, MAE	Visual, PSNR, SSIM, MAE	128×128×32
Liu et al. [2020b]	MRI, CT	21 cancer hepatocellular	dense CycleGAN	Adv, L1.5, Gradient Difference	MAE, PSNR, NCC, HU	64×64×64
Lei et al. [2020a]	MRI, CT	45 prostate cancer MRI/CT	CycleGAN	Adv, Cycle consistency	DSC, Sen, Spe, HD, MSD, RMSD, CMD, PVD	64×64×64
Yang et al. [2019]	MRI, CT	N/D	N/D (3D-Unet/3D CNN)	Adv, MSE	PSNR, MSE	N/D
Zeng and Zheng [2019]	MRI, CT	50 subjects MRI/CT	hGAN (CycleGAN based)	Adv, MAE	MAE, PSNR, Visual	256×288×32, 256×288×12
Zhang et al. [2019b]	MRI, CT	4496 cardiovascular MRI/CT	CycleGAN	Adv, Cycle and Shape consistency	Visual, S-score, DSC	112×112×86
Zhang et al. [2018]	MRI, CT	4354 contrasted cardiac CT scans	CycleGAN	Adv, Cycle and Shape consistency	Visual, S-score, DSC	86×112×112
Schaefferkoetter et al. [2021]	MRI, CT, PET	60 patients	CycleGAN (Residual-Unet/patchGAN)	MAE, Cycle consistency, Identity, MSE	MSE, PCC, AC	96×96×96
Cai et al. [2019]	MRI, CT, X-rays	Several datasets ⁴⁸	CycleGAN (cGAN/PatchGAN)	LSGAN, Cycle and Shape consistency	Visual, S-score, DSC	80×128×128

⁴⁶BrainWeb

⁴⁷Data and code available upon request

⁴⁸ 4354/142 contrasted cardiac CT/MRI, 82/78 pancreatic abdomen CT/MRI scans, mammography X-rays (BCDR, INbreast)

Hu et al. [2022]	MRI, PET	ADNI ⁴⁹	BMGAN(Dense-UNet/Patch-Level)	LSGAN, KL-divergence constraint, MAE, Perceptual (VGG-16 ⁵⁰)	MAE, PSNR, MS-SSIM, FID	128×128×128
Lin et al. [2021] ⁵¹	MRI, PET	ADNI ⁴⁷	RevGAN	Adv, Cycle consistency	SSIM, PSNR	96×96×48
Pan et al. [2019]	MRI, PET	ADNI ⁴⁷	FGAN	Adv, Feature-Consistent	MAE, PSNR, SSIM, AUC	N/D
Yan et al. [2018]	MRI, PET	ADNI ⁴⁷	cGAN	Adv, MAE	Visual, SSIM, Acc, AUC	160×160×96

Table 4: Compact overview of reviewed studies with other modalities, sorted by modality and then by year of publication, indicating the modality, and the datasets used with the respective localisation, if available. It also shows the network used, the loss functions, the evaluation metrics, the resolution of the synthetic data generated, and whether or not it is a medical application. The abbreviations used in this table can be found in List 4 or in Section 1.1 (Acronyms and Abbreviations)

Study	Modality	Med	Dataset	Network (G/D)	Loss function	Metrics	Comments
Muzahid et al. [2021]	CAD	No	ModelNet10/40 ⁵²	PC-GAN (PG-GAN/cGAN based)	Adv, Acc	Visual, Acc, Clustering	32×32×32
Greminger [2020]	CAD	No	Synthetic data generated by CadQuery ⁵³	MSG-GAN	Hinge	Compliance, Fraction of Unmachinable Voxels	32×32×32
Kniaz et al. [2020] ⁵⁴	CAD	No	SyntheticVoxels ⁵⁵ , VoxelCity ⁵⁶	Z-GAN (pix2pix based)	MAE, Adv	IoU	128×128×128, Voxel/ PC
Li et al. [2019]	CAD	No	ShapeNet ⁵⁷ , Pix3D ⁵⁸ , Stanford car ⁵⁹ , CUB-Birds-200-2011 ⁶⁰	MP-GAN	Adv	FID, Acc	64×64×64

⁴⁹ADNI

⁵⁰Hu et al. [2022]

⁵¹Code available upon request

⁵²ModelNet10/40

⁵³CadQuery

⁵⁴Z-GAN

⁵⁵SyntheticVoxels

⁵⁶VoxelCity

⁵⁷ShapeNet

⁵⁸Pix3D

⁵⁹Stanford car

⁶⁰CUB-Birds-200-2011

Yang et al. [2017] ⁶¹	CAD	No	ModelNet40 ⁵⁰	3D-RecGAN	Modified CE, WGAN-GP	IoU, CE	64×64×64, Voxel/ PC
Wang et al. [2017] ⁶²	CAD, RGB-D	No	Real-world scans ⁶³ , ModelNet10/40 ⁵⁰	ED-GAN (cGAN based)	Adv, CE, MAE	CE, Acc	32×32×32, 128×128×128
Sciazko et al. [2021]	FIB-SEM	No	Ni70GDC30, Ni30GDC70, Ni70GDC30(200MPa), Ni30GDC70(200MPa)	GAN2Dto3D	Adv	Average volume fractions, Volume fraction variations, TPB/DPB densities	64×64×64
Gupta et al. [2021] ⁶⁴	Microscopy (cryo-EM)	Yes	EMPIAR-10061 ⁶⁵ EMPIAR-10028 ⁶⁶	CryoGAN (cryo-EM physics simulator)	Adv, WGAN-GP	Reconstruction resolution (Å)	180×180×180
Chen et al. [2021]	Microscopy	Yes	Human kidney	SpCycleGAN	Adv, Cycle consistency, Spatial	DSC, Type-I/Type-II error, Acc, IoU, Pre, Sen, F1	128×128(×128) Pos-processing
Tang et al. [2020]	Microscopy	Yes	Janelia-Fly/Tokyo-Fly ⁶⁷	cGAN	MAE, Adv	PSNR, SSIM	128×128×32
Ho et al. [2019] (Fu et al. [2018])	Microscopy (Fluorescence, two-photon)	Yes	Rat kidney	SpCycleGAN	Adv, MAE, MSE	Pre, Sen, F1	128×128×128
Han et al. [2019b]	Microscopy (Fluorescence, two-photon)	Yes	Rat kidney	SpCycleGAN	Adv, Cycle consistency, Spatial, MSE	MAPE, F1, Sen, Pre	128×128×128, 128×128×32, 64×64×64
Baniukiewicz et al. [2019] ⁶⁸	Microscopy (diSPIM light sheet, LSFM, Confocal microscope)	Yes	Cells (several sources) ⁶⁹	cGAN	MAE, Adv	Visual, F1, Sen, Pre	256×256×66 (stack of 66 images 256×256)
Liu et al. [2021]	RGB-D	No	ModelNet40 ⁵⁰ , KinectData ⁷⁰	DLGAN (ED-GAN)	Adv, Latent vector, Depth	IoU, CE	64×64×64

⁶¹3D-RecGAN

⁶²3D Shape Completion

⁶³Real-world scans

⁶⁴CryoGAN

⁶⁵EMPIAR-10061

⁶⁶EMPIAR-10028

⁶⁷Janelia-Fly/Tokyo-Fly

⁶⁸pix2pix_3D_multichannel

⁶⁹Sources: [here](#), [here](#), [here](#)

⁷⁰KinectData

Liu et al. [2020a]	Seismic reflection data	No	Synthetic model, F3 block seismic data ⁷¹	semi-supervised GANs	Adv, CE, MSE	Acc, F1	64×64×64
Kench and Cooper [2021] ⁷²	Synthetic, x-ray, KPFM, SEM	No	Several materials ⁷³	SliceGAN	Adv, WGAN	Visual, Volume fraction, Relative surface area, Relative diffusivity	64×64×64
Yang et al. [2021a] ⁷⁴	Synthetic (Data simulator, PSF ⁷⁵)	Yes	Synthetic isotropic quad-view embryo and <i>C. elegans</i> ⁷⁶	CycleGAN based (CNN based/multi-scale)	LSGAN, Cycle consistency, MSE	NRMSE, PSNR, SSIM, CC	64×64×64
Nozawa et al. [2021]	Synthetic	No	3D car meshes ⁷⁷ , Contour sketches	cGAN	Adv, MAE, CE	Visual	64×64×Views (reconstruction using several views), Voxel/ PC
Shen et al. [2021]	Synthetic	No	653 3D Strand-level models ⁷⁸	WGAN-GP	WGAN-GP, Content, Style, Laplacian, Projection, Orientation	MSE, Visual	128×128×96
Danu et al. [2019]	Synthetic	Yes	2D/3D vessel-like structures, 3D stenosed blood vessel segments	GAN (N/D)	Adv	Visual	128×128, 64×64×64, 128×32×32, Meshes /Voxel
Halpert [2019]	Synthetic (Earth Model)	No	SEAM Phase I synthetic model ⁷⁹	DCGAN	Adv	Visual	32×32×32

⁷¹F3 block seismic data

⁷²SliceGAN

⁷³See their Table 2

⁷⁴MultiViewFusion

⁷⁵PSF

⁷⁶Synthetic isotropic quad-view embryo and *C. elegans*

⁷⁷3D car meshes

⁷⁸Strand-level models: [here](#), and [here](#)

⁷⁹SEAM Phase I synthetic model

3.5 Applications

This section summarises all works in two different tables, sorted by application. Table 5 contains all medical papers, sorted by application and organ, and Table 6 contains all non-medical papers, also sorted by application and structure. Animal and cell studies were considered medical applications.

In Table 5 it is possible to find the columns: *Application*, *Modality*, *Study*, *Network*, *Organ*, and *Notes*. As specified in the *Organ* column, the cells have several sources, such as kidneys, embryos, neurons, and blood vessels. The last column highlights the main contribution of the paper. *Image translation* is the main application of GANs in a medical context, as can be seen in Figure 6.

Figure 7 shows the number of medical publications sorted by the number of papers on a specific organ. It can be seen that the most studied organ is the brain, followed by the lungs. The study of 3D structures of cells with GANs is also very popular. Figure 13 shows all GAN architectures used in each application. The cGAN architecture is the most commonly used architecture in various applications, but it can be seen that CycleGAN-based architectures are the preferred choice for image translation and multimodal data.

The application "General" refers to the use of GANs only for the generation of synthetic data without a specific purpose, or that only proposals are presented but not developed in the papers.

Table 6 has the columns: *Application*, *Modality*, *Study*, *Network*, and *Structure*. The last column contains the objects used in the study, although in some cases different objects are used, so it is simply written *Objects* or *Models*. The number of papers per application is shown in Figure 6, where *Reconstruction* is the main application of GANs in a non-medical context.

Table 5: Compact overview of reviewed medical papers sorted by application, then by modality and year. The application, the studied organ and the highlights/notes are the main purpose of this table

Application	Modality	Study	Network	Organ	Notes
Classification	CT	Bu et al. [2021]	cGAN (3D-Unet/ 3D CNN)	Lung	Boost the overall performance of the lung nodule detection network by 2.53%
Classification	CT	Pesaranghader et al. [2021]	CT-SGAN	Lung	Pretraining the nodule detection classifier on synthetic volumes and fine-tuning on the real data
Classification	CT	Han et al. [2019a]	MCGAN (U-NET/ Pix2Pix)	Lung	Generating lung nodules using bounding box and adding surrounding tissues
Classification	Microscopy	Baniukiewicz et al. [2019]	cGAN	Cells	When 3D label is not available, create pseudo-3D synthetic cell data from individually generated 2D slices
Classification	MRI	Dikici et al. [2021]	cGANe (DCGAN based)	Brain	Provide a novel data-sharing protocol
Classification	MRI	Momeni et al. [2021]	conditional Le- sionGAN (cGAN based)	Brain	It can be applied on unseen dataset with different MRI parameters and diseases
Classification	MRI	Jung et al. [2020]	cGAN	Brain	The classification task improved
Classification	MRI	Zhuang and Schwing [2019]	ICW-GAN	Brain	It showed that not all data augmentation methods are equally beneficial
Denoising	OCT	Li et al. [2020]	GAN (N/D)	Brain	This provided more data for noise reduction training
Image translation	CBCT to CT	Qin et al. [2021]	GAN (Residual- Unet/CNN)	Lung	Investigated the dose validation accuracy
Image translation	CBCT to CT (corrected CBCT)	Harms et al. [2019]	res-cycle GAN	Brain, Pelvis	CBCT allows for daily 3D imaging, for enhanced image-guided radiation therapy
Image translation	CT to CBCT	Wei et al. [2020]	cGAN	Lung	Handle the discrepancy between the DRR from CT and an x-ray projection
Image translation	CT and Low count PET to full count PET	Lei et al. [2020b]	CycleGAN	Whole Body	This technique could be a useful tool for low dose PET imaging
Image translation	CT to MRI	Yang et al. [2021b]	CAE-ACGAN	Brain	Multi-contrast MR synthesis
Image translation	CT to MRI and vice versa	Gu and Zheng [2021]	Dual3D&Patch- GAN (3DGAN based)	Brain	Creation of a model using transfer learning approach
Image translation	CT to MRI	Lei et al. [2020a]	CycleGAN	Prostate, Bladder, Rectum	Facilitate routine prostate-cancer radiotherapy treatment planning

Image translation	CT to MRI vice versa	Cai et al. [2019]	CycleGAN (cGAN/Patch-GAN)	Heart, Pancreas, Breast	Cross-modality to improve segmentation of multiple data sources in an online manner
Image translation	CT to MRI and vice versa	Zhang et al. [2018, 2019b]	CycleGAN	Heart	Multiclass segmentation using online synthetic data generation
Image translation	MRI to CT	Schaefferkoetter et al. [2021]	CycleGAN (Residual-Unet/patchGAN)	Whole Body	The synthetic CT data used for PET attenuation correction
Image translation	MRI to CT	Liu et al. [2020b]	dense CycleGAN	Liver	Use MRI-only photon or proton radiotherapy treatment planning
Image translation	MRI to CT	Zeng and Zheng [2019]	hGAN (CycleGAN based)	Brain	Less data and computational resources needed due to hybrid approach
Image translation	MRI to PET	Hu et al. [2022]	BMGAN(Dense-UNet/Patch-Level)	Brain	Preserves the diverse brain structure details
Image translation	MRI to PET and vice versa	Lin et al. [2021]	RevGAN	Brain	It uses only one bidirectional generator
Image translation	MRI to PET	Pan et al. [2019]	FGAN	Brain	Achieves the state-of-the-art performance in AD identification and MCI conversion prediction
Image translation	MRI to PET	Yan et al. [2018]	cGAN	Brain	The MCI progression classification improved 7%
Nuclei counting	Microscopy	Han et al. [2019b]	SpCycleGAN	Cells (Kidney)	The method is capable of counting nuclei in 3D
Reconstruction (2D ->3D)	Microscopy	Gupta et al. [2021]	CryoGAN (cryo-EM physics simulator)	Biomolecule	CryoGAN currently achieves a 10.8Å resolution on a realistic synthetic dataset
Reconstruction (2D ->3D)	Synthetic	Yang et al. [2021a]	CycleGAN based (CNN based/multi-scale)	Cells (Embryos)	3D multi-view deconvolution and fusion using semi- and self-supervised networks
Reconstruction (Low ->High)	CT (CTP)	Moghari et al. [2019]	cGAN	Brain	This method could allow dose reduction in CT Perfusion
Segmentation	CT	Zhang et al. [2021]	PGGAN	Pelvis	Semi-supervised learning for semantic segmentation
Segmentation	Microscopy	Chen et al. [2021]	SpCycleGAN	Cells (Kidney)	The non-ellipsoidal nuclei approach achieves improved segmentation on volumes with irregularly shaped nuclei
Segmentation	Microscopy	Ho et al. [2019]	SpCycleGAN	Cells (Kidney)	It can segment nuclei visually and numerically
Segmentation	Microscopy	Tang et al. [2020]	cGAN	Cells (Neuron)	It improves the performance of neuron segmentation

Segmentation	MRI	Ma et al. [2020]	da-GAN	Brain	It can improve Hippocampal subfields segmentation accuracy
Segmentation	MRI and CT	Yang et al. [2019]	N/D (3D-Unet/3D CNN)	Heart	Helps to achieve better understanding cardiovascular motion
General	CT	Xu et al. [2019]	MCGAN	Lung	More vigorous study is needed to verify
General	MRI	Rusak et al. [2020]	GAN (Pix2Pix based)	Brain	Generate brain MRI with accurate borders between tissue
General	MRI	Baumgartner et al. [2018]	VA-GAN (WGAN based 3D U-Net / C3D)	Brain	It can capture multiple regions affected by disease
General	Synthetic	Danu et al. [2019]	GAN (N/D)	Cells (Blood vessels)	The synthetic blood vessels are indistinguishable from the real ones

Table 6: Compact overview of reviewed non-medical papers sorted by application, then by modality and year. The application and the studied structure are the main purpose of this table

Application	Modality	Study	Network	Structure
Classification	CAD	Muzahid et al. [2021]	PC-GAN (PG-GAN/cGAN based)	Objects ⁸⁰
Classification	CAD	Greminger [2020]	MSG-GAN	Models ⁸¹
Classification	Seismic reflection data	Liu et al. [2020a]	semi-supervised GANs	Seismic facies
Reconstruction (2D ->3D)	CAD	Kniaz et al. [2020]	Z-GAN (pix2pix based)	Cars
Reconstruction (2D ->3D)	CAD	Li et al. [2019]	MP-GAN	Objects ⁷⁸
Reconstruction (2D ->3D)	CAD	Yang et al. [2017]	3D-RecGAN	Objects ⁷⁸
Reconstruction (2D ->3D)	CT	Krutko et al. [2019]	SPGAN (3D DCGAN based)	Porous Media
Reconstruction (2D ->3D)	FIB-SEM	Sciazko et al. [2021]	GAN2Dto3D	Electrode
Reconstruction (2D ->3D)	RGB-D	Liu et al. [2021]	DLGAN (EDGAN)	Objects ⁷⁸
Reconstruction (2D ->3D)	Synthetic	Nozawa et al. [2021]	cGAN	Cars
Reconstruction (2D ->3D)	Synthetic	Shen et al. [2021]	WGAN-GP	Hair
Reconstruction (2D ->3D)	Synthetic, x-ray, KPFM, SEM	Kench and Cooper [2021]	SliceGAN	Electrode

⁸⁰Diversified objects

⁸¹Models to be manufactured

Reconstruction (Low ->High)	CAD, RGB-D	Wang et al. [2017]	ED-GAN (cGAN based)	Objects ⁷⁸
Reconstruction (Low ->High)	Synthetic	Halpert [2019]	DCGAN	Seismic
General	CT	Chen et al. [2020]	WGAN with two discriminators	Porous Media
General	CT (XCT)	Gayon-Lombardo et al. [2020]	DCGAN	Electrode
General	CT	Liu et al. [2019]	DCGAN	Porous Media
General	Micro-CT	Mosser et al. [2017]	DCGAN	Porous Media

3.6 Visual Results

As explained in [Section 3.2](#), visual judgement is currently the most widely used evaluation tool and one of the best for assessing the images produced by GANs. Therefore, almost every publication presents some real and synthetic images that allow the reader to check the realism of the synthetic data. However, in some cases, it is very difficult to assess this realism because the 2D rendering processes of the paper can change the colour, resolution, and other properties of the images, e.g. MRI or CT scans. Some authors make the trained generator or some synthetic data freely available, but others do not, making it difficult for readers to perform visual assessments.

Fortunately, it is usually possible to check the improvements only on the basis of the images provided, as the authors are aware of these limitations. In this section, we present some selected images from some reviewed papers, as they can best reflect the realism of the generated synthetic data. We have selected images related to different organs (medical domain) and different structures (non-medical domain).

Figure 14 shows the cGANe system developed by [Dikici et al. \[2021\]](#). They offer a novel protocol for sharing data by generating synthetic data from the original dataset, validating it and making it available at client sites. This inherent anonymization capacity of GANs was already explored by [Shin et al. \[2018\]](#).

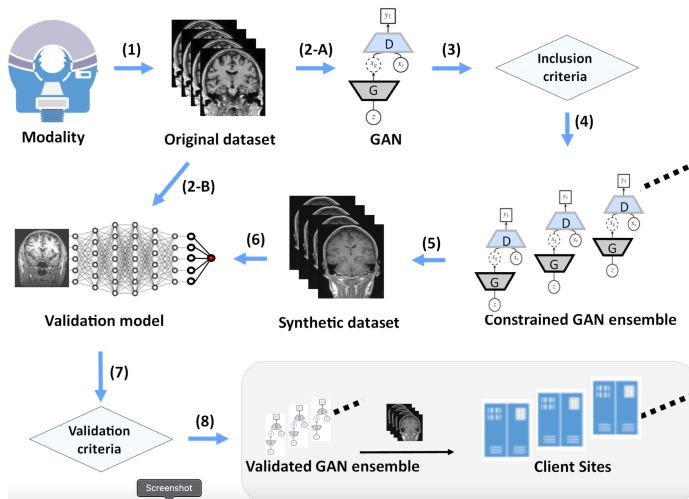


Figure 14: Constrained GAN ensemble for data sharing [Dikici et al. \[2021\]](#).

The error images are used in Figure 15 to help the

readers identify the differences between the ground truth, a scan generated by the proposed method, and two others generated by a 3D Fully Convolutional Neural network and a vanilla GAN. The whiter the error images are, the more similar the synthetic and the original images. In image translation with paired images, this comparison is possible because ground truth is available. However, some authors choose not to use these error images, as can be seen in 16 and 17. In some situations, it is not possible to create them, e.g., when ground truth is not available [Zeng and Zheng \[2019\]](#).

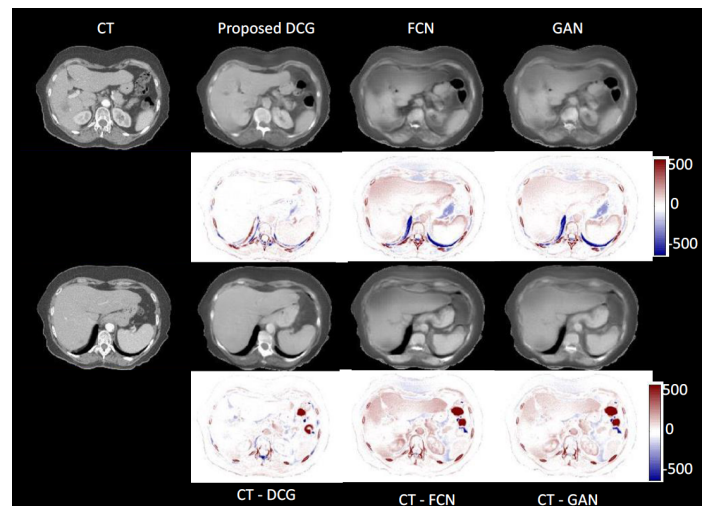


Figure 15: Original axial CT images and synthetic CT images generated by dense-cycle-GAN (DCG) developed by [Liu et al. \[2020b\]](#), 3D Fully Convolutional Neural network (FCN) and vanilla GAN. The second and last rows are the difference image between original CT and the generated CT images.

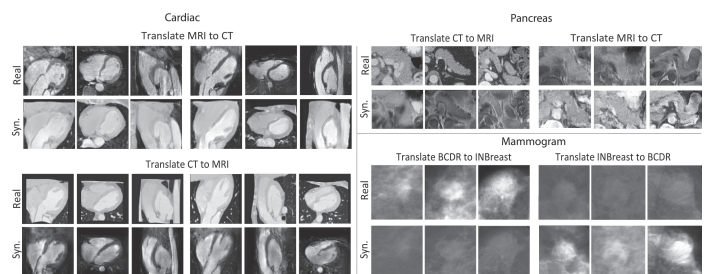


Figure 16: On the left side three orthogonal sections through the centre of the 3D cardiac volumes are shown. The top right displays the pancreatic volumes of the maximum cross-sectional area. The bottom right shows real and synthetic mammographic lesion patches [Cai et al. \[2019\]](#).

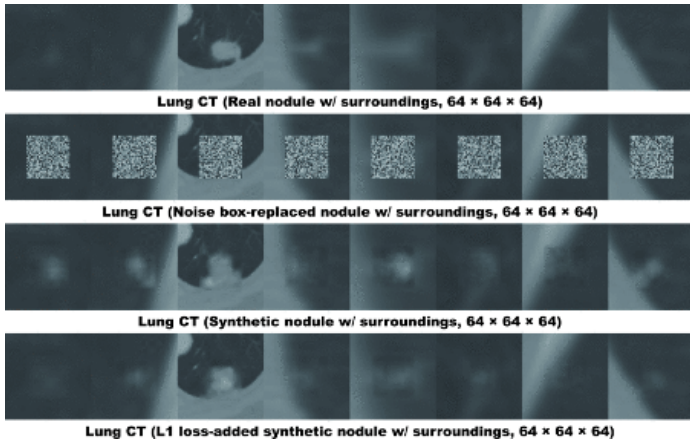


Figure 17: 2D axial view of: First row — Real nodules; Second row — Lung nodules replaced by noise of dimension $32 \times 32 \times 32$; Third row — Synthetic nodules with surrounding tissue; Fourth row — Synthetic nodules using L_1 loss with surrounding tissue [Han et al. \[2019a\]](#).

If the generation of synthetic data is only an intermediate step, this visual analysis is not very important if it is successful in its purpose. [Han et al. \[2019a\]](#) improved the nodule detection algorithm by using synthetic data. Figure 17 shows the results of generating synthetic nodules and inserting them into surrounding tissue with and without using the L_1 loss. In this case, it is possible to see the differences between the two approaches.

[Lei et al. \[2020a\]](#) trained a CycleGAN-based architecture to perform image translation from CT to MRI to achieve better soft tissue contrast. Again, the focus of this work is not on the realism of synthetic MRIs, but on improving segmentation when synthetic data are available. In Figure 18 it can be seen that the segmentation performed with synthetic data outperforms the other two when compared to manual segmentation (a3).

The CycleGAN architecture is so versatile that it can also be used for image translation in small structures such as the heart, pancreas, and mammograms, as seen in Figure 16 by [Cai et al. \[2019\]](#). It can even be used for translating whole body images, as shown in Figure 19 developed by [Lei et al. \[2020b\]](#).

Still in the medical field, GANs have been used successfully by [Danu et al. \[2019\]](#) to generate stenosed segments of coronary arteries and by [Gupta et al. \[2021\]](#) to generate reconstructions of the 80S Ribosome, as seen in Figures 20 and 21. This last work dif-

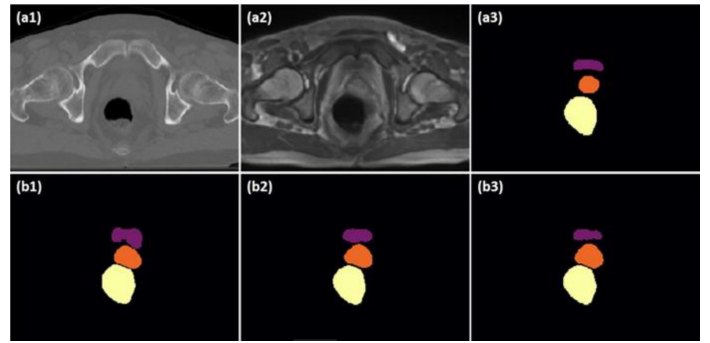


Figure 18: Comparison between original and synthetic scans generated by the method proposed by [Lei et al. \[2020a\]](#), and segmentations: (a1) CT image; (a2) synthetic MRI; (a3) manual segmentation of bladder, prostate, and rectum. (b1) segmentation by DSU-net; (b2) segmentation by DAU-net trained on CT data; (b3) segmentation by DAU-net trained on synthetic MRI data.

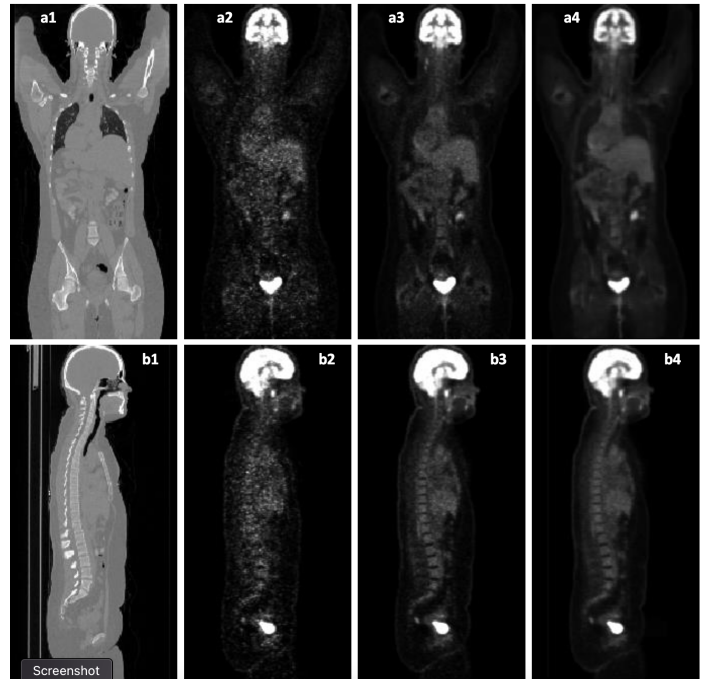


Figure 19: Visual results. (a1-a4) shows the sagittal views of CT, low count PET, full count PET and synthetic full count PET images. (b1-b4) shows the coronal views [Lei et al. \[2020b\]](#).

fers from the others because a CryoEM physics simulator was used as a generator instead of a deep learning architecture.

The use of GANs to generate 3D data is not limited to medical imaging, as explained earlier. They can also be used to generate synthetic porous media or 3D

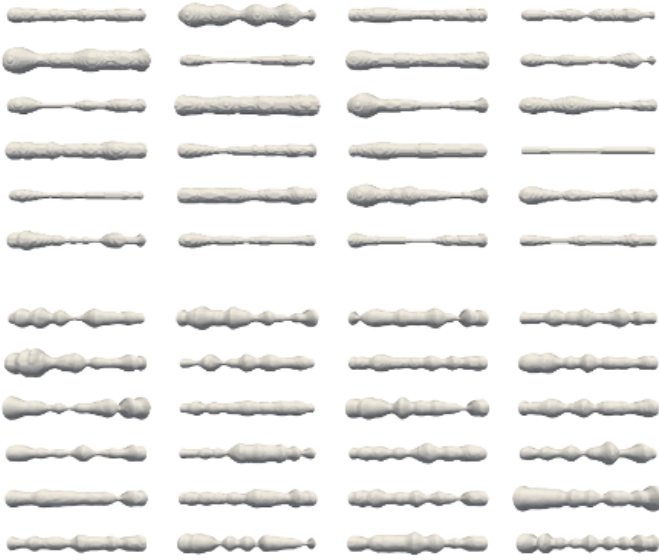


Figure 20: Stenosed segments of coronary arteries [Danu et al. \[2019\]](#): Top — training surfaces; Bottom — synthetically generated using the GAN model.

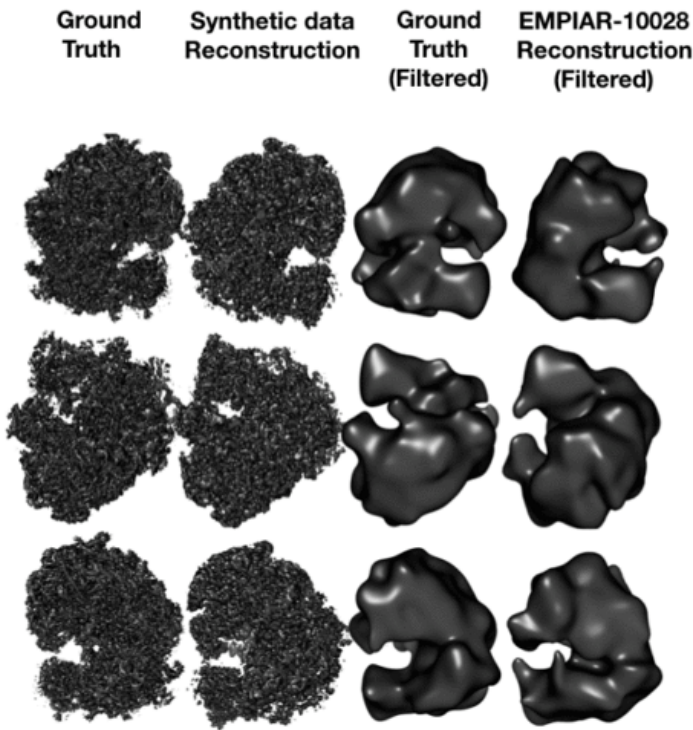


Figure 21: Different views of the 80S Ribosome and reconstruction using CryoGAN [Gupta et al. \[2021\]](#). First column — 80S Ribosome from EMPIAR-10028; Second column — CryoGAN reconstruction from synthetic data with; Third column — 80S Ribosome filtered; Fourth column — CryoGAN reconstruction filtered.

car shapes from sketches, as shown in Figures 22 and 23, or even various everyday objects [Muzahid et al. \[2021\]](#). These works demonstrate the wide versatility of GAN architectures.

It would be beneficial to the paper if in addition to the error images, the authors also represented the evolution of training, as made by [Liu et al. \[2019\]](#) and shown in Figure 23. It is known that the GANs training is very unstable and during training the output may deteriorate, but if no training breakdown occurs, such as mode collapse, the discriminator will eventually improve the output of the generator.

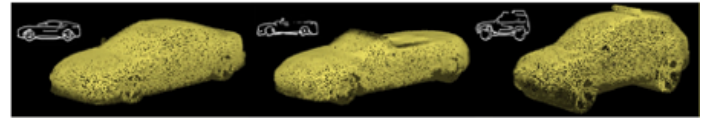


Figure 22: Examples of 3D car shapes generated by the system created by [Nozawa et al. \[2021\]](#) with side-view sketches. Top left white lines are input contour sketches; blue point clouds are corresponding outputs.

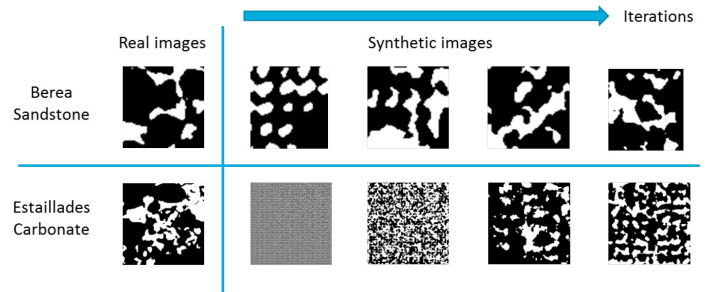


Figure 23: Real and generated images during training process for Berea sandstone and Estailades carbonate sample [Liu et al. \[2019\]](#).

4 Discussion and Conclusion

Using GANs to generate volumetric data has become a highly researched topic, although it was not explored much in the first two years of the existence of GANs. This review has shown that GANs are capable of generating synthetic data that can be used for various medical and non-medical purposes. However, the generation of volumetric data is of great importance for the medical field, as volumetric medical imaging such as CT, MRI, and PET is increasingly being used, and the need for suitable pipelines to pro-

cess these data is growing. Problems such as classification, segmentation or even reconstruction have already been heavily studied, both for medical and non-medical fields.

Other papers: The authors are aware of a few relevant papers that were not covered by the systematic review search. However, they are worth mentioning because of their novel results.

Ferreira et al. [2022a] and Ferreira et al. [2022b] developed a pipeline for generating synthetic rat brain MRIs by relying on the alpha-GAN architecture Rosca et al. [2017]; Kwon et al. [2019], but with two different goals in mind. The first work addressed the need of large datasets to train deep learning models and a solution to this challenge, i.e. the use of GANs. They proved that it is possible to use synthetic data generated by GANs to improve existing segmentation algorithms. The second paper went even further and proved that synthetic data can outperform the use of conventional data augmentation and showed that in this particular case conventional data augmentation is actually suboptimal. As far as we know, these are the first papers in which synthetic MRI scans of rat brains have been generated. This work is the evidence that GANs can also be used in preclinical studies.

Sun et al. [2020] proposes an architecture based on GANs to solve the limited amount of labelled datasets. The MM-GAN can translate label maps into 3D MRI without distorting the pathology. They proved the extensibility of their approach by using the BraTS17 dataset and a new dataset (LIVER100).

Tendencies of 3D volume data generating with GANs:

Most of the works use existing GAN architectures that have been adapted and improved for the problem at hand. Architectures such as CycleGAN, cGAN, WGAN/WGAN-GP, progressive growing GANs (PGGAN), and DCGAN were first developed for 2D data generation and then adapted to volumetric data. As mentioned earlier, the main state-of-the-art GAN architectures are 2D-related. These works are so remarkable that researchers usually decide to adapt them for volumetric generation instead of trying to achieve such results from scratch.

The use of CycleGAN-based architectures is a preferred choice for many applications, namely image

translation, nuclei counting, reconstruction, and segmentation, as it is not limited to the use of only one modality. Its ability to handle multimodality is a valuable asset that has already been explored, especially for medical data. It is well known that the use of more than one medical modality for diagnosis is widespread, as it offers more information. It is highly desirable to have pipelines that are able to mimic physicians who use more than one modality when treating patients Heiliger et al. [2022]. As shown in Huang et al. [2020], using multimodal data can lead to higher accuracy and better imitate human experts. Therefore, it is only natural that versatile mechanisms capable of handling them are the next steps in which the CycleGAN-based architecture can have a crucial role.

For non-medical applications, cGAN and deep convolutional generative adversarial networks (DCGAN) have been the preferred choice. From this review, it can be seen that volumetric data generation has been applied more to medical data than to non-medical data, limiting the development of the latter. In the majority of papers, authors preferred to keep the use of GAN networks at a simpler level without using more complex networks. While this is not a shortcoming, it would be interesting to use more complex networks to provide deeper conclusions.

Another approach was developed by Han et al. [2019a], that does not generate the entire volume. They created a pipeline to generate lung nodules in the desired position, size and attenuation by creating small volumes (32^3) with nodules and adding them to the surrounding tissue, creating 64^3 volumes. This technique can also be extended to various other types of lesions in other organs by converting the scans from healthy patients to diseased ones. It can also be applied beyond medicine, for example to create a specific porous media between other materials or to create synthetic fractures in materials. This allows saving computational resources and a more stable training due to the small output size of the generator.

It is also noted that latent space has not been explored as much as it should. As explained in Fragemann et al. [2022], the "black box" inherent in generative models should be eliminated by better understanding the models and exploring techniques such as *disentanglement*. Therefore, this deep understanding and exploration can also be the next approach to

the use of GANs, rather than creating new architectures.

CycleGAN-based: In works such as [Zhang et al. \[2018, 2019b\]](#), this technology is used to generate MRI scans from CT and vice versa to increase the amount of data available for multiclass segmentation of the heart. Generating one modality from another is also applied to the liver, brain or even the whole body, as can be seen in table 5, showing the versatility of these architectures. In works such as [Schaefferkoetter et al. \[2021\]](#); [Zeng and Zheng \[2019\]](#); [Zhang et al. \[2019b, 2018\]](#), the use of GANs have proven to be beneficial for exploiting multimodal medical datasets, even when only unpaired data exists.

Challenges: However, many challenges remain, such as those mentioned in **Section 2**. Instability, mode collapse, non-convergence and diminished gradient are even more difficult to overcome when dealing with volumetric data. To process this type of data, computers with high processing and storage capacity are required. Some works address this last challenge and try to solve it. [Nozawa et al. \[2021\]](#) used multiview depth images as an intermediate representation and then created the volume by re-composing multiple views. [Jung et al. \[2020\]](#) replaced the 3D Generator with a 2D Generator, keeping a 3D and a 2D Discriminator, which allowed faster training with lower memory consumption and still good 3D quality. [Pesaranghader et al. \[2021\]](#) was also able to create volumes with dimensions larger than 224^3 by generating several slices and then assembling them instead of processing the entire volume at once.

A consistent metric for comparing different models is also crucial. For example, if two papers use the same data set to generate new data, it is very difficult to compare which model is better. For reconstruction or noise reduction problems, this problem is mitigated by having ground truth available, e.g., in [Harms et al. \[2019\]](#); [Lei et al. \[2020b\]](#); [Liu et al. \[2020b\]](#); [Li et al. \[2020\]](#), as the use of PSNR is widely accepted, but for modality generation [Lei et al. \[2020b\]](#), it is very difficult to use only unpaired data, or when the goal is to generate new scans [Xu et al. \[2019\]](#). Even quality control through human judgement is a bottleneck, as the developer may not have the required expertise in the field at hand, e.g. medical image analysis, and

relies on expert feedback, which is difficult to obtain, very expensive, and time-consuming.

GANs can also be a threat, as they can be used to deceive people. Recently, there have been increasing reports of the use of synthetic videos and voices in video calls ⁸². This technology can be harmful, but it can also be used to combat them.

Research Questions:

1. What are the different applications of GANs in the generation of volumetric data?

GANs are used in various fields, whereby a distinction can be made between medical and non-medical fields, since most works are in the medical field. They can be used for classification, reconstruction, denoising, nuclei counting, segmentation, image translation and general purposes, as can be seen in Tables 5 and 6.

2. What are the methods most frequently or successfully employed by GANs in the generation of volumetric data?

Since it is not possible to make a good comparison between the models, it is not easy to assert which GANs are more successful in generating volumetric data. However, CycleGAN-based architectures are chosen very often and have achieved good results, followed by architectures based on cGAN, DCGAN, and WGAN / WGAN-GP, as can be seen in Figure 13 and Tables 2, 3 and 4.

3. What are the strengths and limitations of these methods?

The use of GANs has proven to be a powerful tool for handling multimodal data, for data augmentation, and for anonymisation. However, there are several problems that have already been mentioned in the **Remaining problems** section. The lack of a consensus metric to compare GANs, the instability of training, and hardware limitation remain major challenges, especially when dealing with volumetric data.

4. What improvements are sought through the use of this technology?

⁸²[Deepfakes new](#)

This technology is widely used to generate anonymised synthetic data for data augmentation, as shown in this review, due to the inherent anonymisation capacity of GANs and because of its realism compared to other generative approaches. The synthetic data can be used to improve other Deep Learning algorithms by solving the problem of lack of data and being a good aid for other data augmentation techniques. In addition, GANs can also be used for denoising, reconstruction and modality translation problems, making these architectures a powerful tool to have always ready when other technologies are not satisfactory.

Conclusion: In this systematic review, we give an overview of GAN-based approaches for the generation of realistic 3D data. In doing so, we group the screened works by the underlying data (dimension), which can be 2D or 3D. Then, we further group them by the targeted modalities, like 3D models, CT, MRI, PET, or combinations of modalities. We furthermore extracted the used datasets and if they are public ones that are available to the research community, or if these are so-called private or in-house repositories that are not (yet) available to the community. Note that even if making datasets available alongside publications is becoming more and more common these days, there may be reasons for keeping data under lock. Making data, especially medical data, public requires much more efforts and extended or additional ethics approvals. It can also be that the institution that generated the data, e.g. a hospital, allows studying the data but forbids its publication, or that the disease is so rare in the institution that it does not make sense to publish it because only a few cases are involved. Another reason can be, that the authors want first to exploit the data for further studies and publications, e.g. for rare disease cases, which can be understandable, because creating data collections requires a certain amount of effort, especially large ones, including further manual processing such as creating ground truth segmentations. Getting an internal review board to share the data with internal and external partners involved in the study also takes time and a lot of work, with regard to preparation and anonymisation.

In addition to the datasets and modalities, we ex-

tracted the data types, the network architectures, the loss functions, evaluation metrics and resolutions for every reviewed work. It was concluded that the main modality used was CT, followed by MRI, and that the use of multimodal data is widely used specially in the medical context. *Image translation* was the main use of GANs, followed by *Reconstruction*, which explains the extensive use of CycleGAN-based and cGAN-based architectures. It can be seen that, especially in the non-medical context, the use of synthetically generated datasets to train GANs was a trend in the last year (2021). In the medical context, the use of multimodal data has been explored every year, proving the importance and need for appropriate pipelines to process this type of data.

Research Opportunities: GANs could be used to generate synthetic head scans of faces, as defacing head scans is not always an option, e.g., for medical Augmented Reality [Gsaxner et al. \[2019\]](#) and facial implants [Memon et al. \[2021\]](#). In these works, it is not possible to develop algorithms with satisfactory results once it is very difficult to obtain large datasets with the face part, especially with the soft tissue. All data must be accepted so that it can be published and freely shared, but data like this are very difficult to accept because they are not anonymous since they have the face part. Therefore, generating synthetic faces for these scans would be a good solution to this challenge.

The creation and deployment of a full data anonymisation framework could be a good solution to data sharing problems, as proposed by [Shin et al. \[2018\]](#). It would also be very interesting to develop a tool that is able to automate the whole process of training and generating synthetic data, similar to the nnUNet [Isensee et al. \[2021\]](#), which is able to configure itself and choose the best network architecture, training, pre- and post-processing for each new task.

The use of multimodal data as input is a little addressed topic. An example of the benefits of using multimodal data is [Lei et al. \[2020b\]](#), which generates a full PET count from low-count PET and CT scans. There are several works that include multimodal data in the training dataset, but they are used to train an image translator and do not exploit the full potential that this dataset can offer, i.e. they only use one modality at a time. For example, the use of PET+CT

scans to produce MRI could be relevant.

In order to improve GANs, a uniform evaluation metric should be established to allow better comparison between models from different studies. It would also be very important to find a metric that is close to human judgment to improve the results of GANs, especially when volumetric data is used. FID adaptation to volumetric problems is not generally accepted because it is computationally intensive and lacks spatial context. Research in this area is more important than the development of new GAN architectures, as several different architectures are already available that show great potential but lack appropriate metrics and loss functions. The next developments of GANs can also proceed through the exploration of latent space and use more techniques such as *disentanglement*. In a medical context, the best approaches will probably be the use of multimodal data, which makes CycleGAN-based architectures highly preferable.

Acknowledgement

This work received funding from enFaced (FWF KLI 678), enFaced 2.0 (FWF KLI 1044) and KITE (Plattform für KI-Translation Essen) from the REACT-EU initiative (<https://kite.ikim.nrw/>).

References

- Alqahtani, H., Kavakli-Thorne, M., Kumar, G., 2021. Applications of generative adversarial networks (gans): An updated review. *Archives of Computational Methods in Engineering* 28, 525–552.
- Amirrajab, S., Abbasi-Sureshjani, S., Al Khalil, Y., Lorenz, C., Weese, J., Pluim, J., Breeuwer, M., 2020. XCAT-GAN for Synthesizing 3D Consistent Labeled Cardiac MR Images on Anatomically Variable XCAT Phantoms. *Lecture Notes in Computer Science (including subseries Lecture Notes in Artificial Intelligence and Lecture Notes in Bioinformatics)* 12264 LNCS, 128–137. URL: https://www.scopus.com/inward/record.uri?eid=2-s2.0-85092792431&doi=10.1007/978-3-030-59719-1_13&partnerID=40&md5=f43710a34b87f543f84ede879eaa49a9, doi:10.1007/978-3-030-59719-1_13, arXiv:2007.13408.
- Apostolopoulos, I.D., Papathanasiou, N.D., Apostolopoulos, D.J., Panayiotakis, G.S., 2022. Applications of generative adversarial networks (gans) in positron emission tomography (pet) imaging: A review. *European Journal of Nuclear Medicine and Molecular Imaging*, 1–23.
- Arjovsky, M., Chintala, S., Bottou, L., 2017. Wasserstein GAN URL: <http://arxiv.org/abs/1701.07875>, arXiv:1701.07875.
- Arora, A., Shantanu, 2020. A review on application of gans in cybersecurity domain. *IETE Technical Review*, 1–9.
- Baek, S., Kim, K.I., Kim, T.K.T.K., 2020. Weakly-Supervised Domain Adaptation via GAN and Mesh Model for Estimating 3D Hand Poses Interacting Objects, in: *Proceedings of the IEEE Computer Society Conference on Computer Vision and Pattern Recognition*, pp. 6120–6130. URL: <https://www.scopus.com/inward/record.uri?eid=2-s2.0-85095521528&doi=10.1109/2FCVPR42600.2020.00616&partnerID=40&md5=a11d95e96da1220920ec99fd040e45b1>, doi:10.1109/CVPR42600.2020.00616.
- Baniukiewicz, P., Lutton, E.J., Collier, S., Bretschneider, T., 2019. Generative Adversarial Networks for Augmenting Training Data of Microscopic Cell Images. *Frontiers in Computer Science* 1, 1–12. URL: <https://www.scopus.com/inward/record.uri?eid=2-s2.0-85096800557&doi=10.3389/2Ffcomp.2019.00010&partnerID=40&md5=e738206c185a6a2e88ac239c08dc76cb>, doi:10.3389/fcomp.2019.00010.
- Baratloo, A., Hosseini, M., Negida, A., El Ashal, G., 2015. Part 1: simple definition and calculation of accuracy, sensitivity and specificity.
- Baumgartner, C.F., Koch, L.M., Tezcan, K.C., Ang, J.X., Konukoglu, E., 2018. Visual Feature Attribution Using Wasserstein GANs, in: *Proceedings of the IEEE Computer Society Conference on Computer Vision and Pattern Recognition, IEEE*. pp. 8309–8319. URL: <https://www.scopus.com/inward/record.uri?eid=2-s2.0-85050319673&doi=10.1109/2FCVPR.2018.00867&partnerID=40&md5=e4f03dfd7f76d63352f5a911dcb07f0c>, doi:10.1109/CVPR.2018.00867, arXiv:1711.08998.

- Bezerra, H.G., Costa, M.A., Guagliumi, G., Rollins, A.M., Simon, D.I., 2009. Intracoronary optical coherence tomography: a comprehensive review: clinical and research applications. *JACC: Cardiovascular Interventions* 2, 1035–1046.
- Bird, D., Nix, M.G., McCallum, H., Teo, M., Gilbert, A., Casanova, N., Cooper, R., Buckley, D.L., Sebag-Montefiore, D., Speight, R., Al-Qaisieh, B., Henry, A.M., 2021. Multicentre, deep learning, synthetic-CT generation for ano-rectal MR-only radiotherapy treatment planning. *Radiotherapy and Oncology* 156, 23–28. URL: <https://doi.org/10.1016/j.radonc.2020.11.027><https://www.scopus.com/inward/record.uri?eid=2-s2.0-85097718739&doi=10.1016%2Fj.radonc.2020.11.027&partnerID=40&md5=c77495cefa6ffa87a354311ea7dbbcb5>, doi:10.1016/j.radonc.2020.11.027.
- Bittner, K., D'Angelo, P., Körner, M., Reinartz, P., 2018. DSM-to-LoD2: Spaceborne stereo digital surface model refinement. *Remote Sensing* 10. URL: <https://www.scopus.com/inward/record.uri?eid=2-s2.0-85058873455&doi=10.3390%2Frs10121926&partnerID=40&md5=cf5f2747c86413742836895228bd3a38>, doi:10.3390/rs10121926.
- Boehm, H., Fink, C., Attenberger, U., Becker, C., Behr, J., Reiser, M., 2008. Automated classification of normal and pathologic pulmonary tissue by topological texture features extracted from multi-detector ct in 3d. *European radiology* 18, 2745–2755.
- Bongini, F., Berlincioni, L., Bertini, M., Del Bimbo, A., 2021. Partially Fake it Till you Make It: Mixing Real and Fake Thermal Images for Improved Object Detection, in: *MM 2021 - Proceedings of the 29th ACM International Conference on Multimedia*, Association for Computing Machinery. pp. 5482–5490. URL: <https://www.scopus.com/inward/record.uri?eid=2-s2.0-85119343071&doi=10.1145%2F3474085.3475679&partnerID=40&md5=ea2e623d48ecb2ee20b6298a6dfd0bac>, doi:10.1145/3474085.3475679, arXiv:2106.13603.
- Brock, A., Donahue, J., Simonyan, K., 2019. Large scale GAN training for high fidelity natural image synthesis. 7th International Conference on Learning Representations, ICLR 2019 , 1–35 arXiv:arXiv:1809.11096v2.
- Brundage, M., Avin, S., Clark, J., Toner, H., Eckersley, P., Garfinkel, B., Dafoe, A., Scharre, P., Zeitzoff, T., Filar, B., et al., 2018. The malicious use of artificial intelligence: Forecasting, prevention, and mitigation. arXiv preprint arXiv:1802.07228 .
- Bu, T., Yang, Z., Jiang, S., Zhang, G., Zhang, H., Wei, L., 2021. 3D conditional generative adversarial network-based synthetic medical image augmentation for lung nodule detection. *International Journal of Imaging Systems and Technology* 31, 670–681. URL: <https://www.scopus.com/inward/record.uri?eid=2-s2.0-85092452586&doi=10.1002%2Fima.22511&partnerID=40&md5=7c94b491f74669dd9d45a327401e9019>, doi:10.1002/ima.22511.
- Cai, J., Zhang, Z., Cui, L., Zheng, Y., Yang, L., 2019. Towards cross-modal organ translation and segmentation: A cycle- and shape-consistent generative adversarial network. *Medical Image Analysis* 52, 174–184. URL: <https://doi.org/10.1016/j.media.2018.12.002><https://www.scopus.com/inward/record.uri?eid=2-s2.0-85058820733&doi=10.1016%2Fj.media.2018.12.002&partnerID=40&md5=1c09ba30fd56a1bf180766f6bc93e7be>, doi:10.1016/j.media.2018.12.002.
- Chen, A., Wu, L., Han, S., Salama, P., Dunn, K.W., Delp, E.J., 2021. Three dimensional synthetic non-ellipsoidal nuclei volume generation using bézier curves, in: *Proceedings - International Symposium on Biomedical Imaging*, pp. 961–965. URL: <https://www.scopus.com/inward/record.uri?eid=2-s2.0-85107177108&doi=10.1109%2FISBI48211.2021.9434149&partnerID=40&md5=60d095aa52a370294780a6b9bdfc1087>, doi:10.1109/ISBI48211.2021.9434149.
- Chen, H., 2021. Challenges and corresponding solutions of generative adversarial networks (gans): a survey study, in: *Journal of Physics: Conference Series*, IOP Publishing. p. 012066.
- Chen, L., Li, S., Guo, C., 2020. Using Ternary Adversarial Networks to Capture Geometric Information in the Reconstruction of Porous Media,

- in: 2020 IEEE MTT-S International Conference on Numerical Electromagnetic and Multiphysics Modeling and Optimization, NEMO 2020, pp. 20–23. URL: <https://www.scopus.com/inward/record.uri?eid=2-s2.0-85101278862&doi=10.1109%2FNEMO49486.2020.9343664&partnerID=40&md5=41c41aab6b6bf976f95e8bf8a9a786d2>, doi:10.1109/NEMO49486.2020.9343664.
- Chen, Y., An, H., 2017. Attenuation correction of pet/mr imaging. *Magnetic Resonance Imaging Clinics* 25, 245–255.
- Collis, R., 1970. Lidar. *Applied optics* 9, 1782–1788.
- Danu, M., Nita, C.I.C.I., Vizitiu, A., Suciu, C., Itu, L.M., 2019. Deep learning based generation of synthetic blood vessel surfaces, in: 2019 23rd International Conference on System Theory, Control and Computing, ICSTCC 2019 - Proceedings, IEEE. pp. 662–667. URL: <https://www.scopus.com/inward/record.uri?eid=2-s2.0-85075085221&doi=10.1109%2FICSTCC.2019.8885576&partnerID=40&md5=6bc66db684eea34a9025ee6d2074d84a>, doi:10.1109/ICSTCC.2019.8885576.
- Dash, A., Gamboa, J.C.B., Ahmed, S., Liwicki, M., Afzal, M.Z., 2017. Tac-gan-text conditioned auxiliary classifier generative adversarial network. arXiv preprint arXiv:1703.06412 .
- De Myttenaere, A., Golden, B., Le Grand, B., Rossi, F., 2016. Mean absolute percentage error for regression models. *Neurocomputing* 192, 38–48.
- Depeursinge, A., Foncubierta-Rodriguez, A., Van De Ville, D., Müller, H., 2014. Three-dimensional solid texture analysis in biomedical imaging: review and opportunities. *Medical image analysis* 18, 176–196.
- Dikici, E., Bigelow, M., White, R.D., Erdal, B.S., Prevedello, L.M., 2021. Constrained generative adversarial network ensembles for sharable synthetic medical images. *Journal of Medical Imaging* 8. URL: <https://www.scopus.com/inward/record.uri?eid=2-s2.0-85105508865&doi=10.1117%2F1.JMI.8.2.024004&partnerID=40&md5=a294c29d8e16c4a6234ed74e0e06fd43>, doi:10.1117/1.JMI.8.2.024004.
- Dumay, J., Fournier, F., 1988. Multivariate statistical analyses applied to seismic facies recognition. *Geophysics* 53, 1151–1159.
- Egger, J., Gsaxner, C., Pepe, A., Pomykala, K.L., Jonske, F., Kurz, M., Li, J., Kleesiek, J., 2022. Medical deep learning—a systematic meta-review. *Computer Methods and Programs in Biomedicine* , 106874.
- Egger, J., Pepe, A., Gsaxner, C., Jin, Y., Li, J., Kern, R., 2021. Deep learning—a first meta-survey of selected reviews across scientific disciplines, their commonalities, challenges and research impact. *PeerJ Computer Science* 7, e773.
- Fadero, T.C., Gerbich, T.M., Rana, K., Suzuki, A., DiSalvo, M., Schaefer, K.N., Heppert, J.K., Boothby, T.C., Goldstein, B., Peifer, M., et al., 2018. Lite microscopy: Tilted light-sheet excitation of model organisms offers high resolution and low photobleaching. *Journal of Cell Biology* 217, 1869–1882.
- Ferreira, A., Magalhães, R., Alves, V., 2022a. Generation of synthetic data: A generative adversarial networks approach, in: *Big Data Analytics and Artificial Intelligence in the Healthcare Industry*. IGI Global, pp. 236–261.
- Ferreira, A., Magalhães, R., Mériaux, S., Alves, V., 2022b. Generation of synthetic rat brain mri scans with a 3d enhanced alpha generative adversarial network. *Applied Sciences* 12, 4844.
- Fischer, A.C., Mäntysalo, M., Niklaus, F., 2020. Inkjet printing, laser-based micromachining, and micro–3d printing technologies for mems, in: *Handbook of silicon based MEMS materials and technologies*. Elsevier, pp. 531–545.
- Flach, P.A., 2010. *ROC Analysis*. Springer US, Boston, MA. pp. 869–875. URL: https://doi.org/10.1007/978-0-387-30164-8_733, doi:10.1007/978-0-387-30164-8_733.
- Fragemann, J., Ardizzone, L., Egger, J., Kleesiek, J., 2022. Review of disentanglement approaches for medical applications—towards solving the gordian knot of generative models in healthcare. arXiv preprint arXiv:2203.11132 .

- Fu, C., Lee, S., Ho, D.J., Han, S., Salama, P., Dunn, K.W., Delp, E.J., 2018. Three dimensional fluorescence microscopy image synthesis and segmentation. IEEE Computer Society Conference on Computer Vision and Pattern Recognition Workshops 2018-June, 2302–2310. doi:10.1109/CVPRW.2018.00298, arXiv:1801.07198.
- Gatys, L.A., Ecker, A.S., Bethge, M., 2016. Image style transfer using convolutional neural networks, in: Proceedings of the IEEE conference on computer vision and pattern recognition, pp. 2414–2423.
- Gayon-Lombardo, A., Mosser, L., Brandon, N.P., Cooper, S.J., 2020. Pores for thought: generative adversarial networks for stochastic reconstruction of 3D multi-phase electrode microstructures with periodic boundaries. npj Computational Materials 6, 1–11. URL: <http://dx.doi.org/10.1038/s41524-020-0340-7><https://www.scopus.com/inward/record.uri?eid=2-s2.0-85086859642&doi=10.1038/2Fs41524-020-0340-7&partnerID=40&md5=c6461f8d1dc13efa34e7829510cd3efe>, doi:10.1038/s41524-020-0340-7, arXiv:2003.11632.
- Ge, C., Gu, I.Y.H.I.H.I.Y.H., Jakola, A.S., Yang, J., 2020. Deep semi-supervised learning for brain tumor classification. BMC Medical Imaging 20, 1–11. URL: <https://www.scopus.com/inward/record.uri?eid=2-s2.0-85088852412&doi=10.1186%2Fs12880-020-00485-0&partnerID=40&md5=a5ffbd1318030de166868ad4407419c9>, doi:10.1186/s12880-020-00485-0.
- Gecer, B., Lattas, A., Ploumpis, S., Deng, J., Papaioannou, A., Moschoglou, S., Zafeiriou, S., 2020. Synthesizing Coupled 3D Face Modalities by Trunk-Branch Generative Adversarial Networks. Lecture Notes in Computer Science (including subseries Lecture Notes in Artificial Intelligence and Lecture Notes in Bioinformatics) 12374 LNCS, 415–433. URL: https://www.scopus.com/inward/record.uri?eid=2-s2.0-85093119230&doi=10.1007%2F978-3-030-58526-6_25&partnerID=40&md5=2555a554453335554de2a36cc6173081, doi:10.1007/978-3-030-58526-6_25, arXiv:1909.02215.
- Goodfellow, I.J., Pouget-Abadie, J., Mirza, M., Xu, B., Warde-Farley, D., Ozair, S., Courville, A., Bengio, Y., 2014. Generative adversarial nets. Advances in Neural Information Processing Systems 3, 2672–2680. arXiv:arXiv:1406.2661v1.
- Gorbatsevich, V.S., Melnichenko, M.A., Vygolov, O., 2019. Enhancing detail of 3D terrain models using GAN, in: Proceedings of SPIE - The International Society for Optical Engineering, p. 46. URL: <https://www.scopus.com/inward/record.uri?eid=2-s2.0-85072571683&doi=10.1117%2F12.2525177&partnerID=40&md5=9b323a7510a190d0e0cf8e4b0fb21574>, doi:10.1117/12.2525177.
- Greminger, M., 2020. Generative adversarial networks with synthetic training data for enforcing manufacturing constraints on topology optimization, in: International Design Engineering Technical Conferences and Computers and Information in Engineering Conference, American Society of Mechanical Engineers. p. V11AT11A005.
- Grosu, A.L., Sprague, L.D., Molls, M., 2006. Definition of Target Volume and Organs at Risk. Biological Target Volume. Springer Berlin Heidelberg, Berlin, Heidelberg. pp. 167–177. URL: https://doi.org/10.1007/3-540-29999-8_13, doi:10.1007/3-540-29999-8_13.
- Gsaxner, C., Wallner, J., Chen, X., Zemmann, W., Egger, J., 2019. Facial model collection for medical augmented reality in oncologic cranio-maxillofacial surgery. Scientific data 6, 1–7.
- Gu, Y., Zheng, Q., 2021. A Transfer Deep Generative Adversarial Network Model to Synthetic Brain CT Generation from MR Images. Wireless Communications and Mobile Computing 2021. URL: <https://www.scopus.com/inward/record.uri?eid=2-s2.0-85105863137&doi=10.1155%2F2021%2F9979606&partnerID=40&md5=f611adb664e107e036786dacb3097f29>, doi:10.1155/2021/9979606.
- Gui, J., Sun, Z., Wen, Y., Tao, D., Ye, J., 2020. A Review on Generative Adversarial Networks: Algorithms, Theory, and Applications 14, 1–28. URL: <http://arxiv.org/abs/2001.06937>, arXiv:2001.06937.
- Gulrajani, I., Ahmed, F., Arjovsky, M., Dumoulin, V., Courville, A., 2017. Improved training of

- wasserstein GANs. *Advances in Neural Information Processing Systems 2017-Decem*, 5768–5778. [arXiv:1704.00028](https://arxiv.org/abs/1704.00028).
- Gupta, H., McCann, M.T., Donati, L., Unser, M., 2021. CryoGAN: A New Reconstruction Paradigm for Single-Particle Cryo-EM Via Deep Adversarial Learning. *IEEE Transactions on Computational Imaging* 7, 759–774. URL: <https://www.scopus.com/inward/record.uri?eid=2-s2.0-85110830435&doi=10.1109%2FTCI.2021.3096491&partnerID=40&md5=c211ffce4699bc0bcfa53083e22f63d0>, doi:10.1109/TCI.2021.3096491.
- Halpert, A.D., 2019. Deep learning-enabled seismic image enhancement, in: 2018 SEG International Exposition and Annual Meeting, SEG 2018, pp. 2081–2085. URL: <https://www.scopus.com/inward/record.uri?eid=2-s2.0-85059390776&doi=10.1190%2Fsegam2018-2996943.1&partnerID=40&md5=2a9067145a1ca9ee64ab560bebdbc359>, doi:10.1190/segam2018-2996943.1.
- Han, C., Kitamura, Y., Kudo, A., Ichinose, A., Rundo, L., Furukawa, Y., Umemoto, K., Li, Y., Nakayama, H., 2019a. Synthesizing Diverse Lung Nodules Wherever Massively: 3D Multi-Conditional GAN-Based CT Image Augmentation for Object Detection, in: *Proceedings - 2019 International Conference on 3D Vision, 3DV 2019, IEEE*. pp. 729–737. URL: <https://www.scopus.com/inward/record.uri?eid=2-s2.0-85075007744&doi=10.1109%2F3DV.2019.00085&partnerID=40&md5=ebde577c6986a556afa17d9f368c2416>, doi:10.1109/3DV.2019.00085, [arXiv:1906.04962](https://arxiv.org/abs/1906.04962).
- Han, S., Salama, P., Dunn, K.W., Delp, E.J., Lee, S., Fu, C., Salama, P., Dunn, K.W., Delp, E.J., 2019b. Nuclei counting in microscopy images with three dimensional generative adversarial networks, in: *Progress in Biomedical Optics and Imaging - Proceedings of SPIE*, p. 105. URL: <https://www.scopus.com/inward/record.uri?eid=2-s2.0-85068333989&doi=10.1117%2F12.2512591&partnerID=40&md5=e96b76e2b56ccb32173ede0aeae88fb>, doi:10.1117/12.2512591.
- Harms, J., Lei, Y., Wang, T., Zhang, R., Zhou, J., Tang, X., Curran, W.J., Liu, T., Yang, X., 2019. Paired cycle-gan-based image correction for quantitative cone-beam computed tomography. *Medical Physics* 46, 3998–4009. doi:10.1002/mp.13656.
- Heiliger, L., Sekuboyina, A., Menze, B., Egger, J., Kleesiek, J., 2022. Beyond medical imaging—a review of multimodal deep learning in radiology.
- Heusel, M., Ramsauer, H., Unterthiner, T., Nessler, B., Hochreiter, S., 2017. GANs trained by a two time-scale update rule converge to a local Nash equilibrium. *Advances in Neural Information Processing Systems 2017-Decem*, 6627–6638. [arXiv:arXiv:1706.08500v6](https://arxiv.org/abs/1706.08500v6).
- Ho, D.J., Han, S., Fu, C., Salama, P., Dunn, K.W., Delp, E.J., 2019. Center-extraction-based three dimensional nuclei instance segmentation of fluorescence microscopy images, in: 2019 IEEE EMBS International Conference on Biomedical and Health Informatics, BHI 2019 - Proceedings, IEEE. pp. 1–4. URL: <https://www.scopus.com/inward/record.uri?eid=2-s2.0-85072997527&doi=10.1109%2FBHI.2019.8834516&partnerID=40&md5=fa8025db72487b52ab4109b4a716bd3d>, doi:10.1109/BHI.2019.8834516, [arXiv:1909.05992](https://arxiv.org/abs/1909.05992).
- Hu, S., Lei, B., Wang, S., Wang, Y., Feng, Z., Shen, Y., 2022. Bidirectional Mapping Generative Adversarial Networks for Brain MR to PET Synthesis. *IEEE Transactions on Medical Imaging* 41, 145–157. URL: <https://www.scopus.com/inward/record.uri?eid=2-s2.0-85113861594&doi=10.1109%2FTMI.2021.3107013&partnerID=40&md5=014b9087441122391100e7d6d64e1a04>, doi:10.1109/TMI.2021.3107013.
- Huang, S.C., Pareek, A., Seyyedi, S., Banerjee, I., Lungren, M.P., 2020. Fusion of medical imaging and electronic health records using deep learning: a systematic review and implementation guidelines. *NPJ digital medicine* 3, 1–9.
- Isensee, F., Jaeger, P.F., Kohl, S.A., Petersen, J., Maier-Hein, K.H., 2021. nnu-net: a self-configuring method for deep learning-based biomedical image segmentation. *Nature methods* 18, 203–211.
- Isola, P., Zhu, J.Y., Zhou, T., Efros, A.A., 2017. Image-to-image translation with conditional adversarial

- networks, in: Proceedings of the IEEE conference on computer vision and pattern recognition, pp. 1125–1134.
- Jeong, J.J., Tariq, A., Adejumo, T., Trivedi, H., Gichoya, J.W., Banerjee, I., 2022. Systematic review of generative adversarial networks (gans) for medical image classification and segmentation. *Journal of Digital Imaging*, 1–16.
- Johnson, J., Alahi, A., Fei-Fei, L., 2016. Perceptual losses for real-time style transfer and super-resolution. *Lecture Notes in Computer Science (including subseries Lecture Notes in Artificial Intelligence and Lecture Notes in Bioinformatics)* 9906 LNCS, 694–711. doi:10.1007/978-3-319-46475-6_43, arXiv:arXiv:1603.08155v1.
- Jung, E., Luna, M., Park, S.H., 2020. Conditional Generative Adversarial Network for Predicting 3D Medical Images Affected by Alzheimer’s Diseases. *Lecture Notes in Computer Science (including subseries Lecture Notes in Artificial Intelligence and Lecture Notes in Bioinformatics)* 12329 LNCS, 79–90. URL: https://www.scopus.com/inward/record.uri?eid=2-s2.0-85092925551&doi=10.1007%2F978-3-030-59354-4_8&partnerID=40&md5=f678b6cb21165b32e0beb456bfc17607, doi:10.1007/978-3-030-59354-4_8.
- Kamalian, S., Lev, M.H., Gupta, R., 2016. Computed tomography imaging and angiography—principles. *Handbook of clinical neurology* 135, 3–20.
- Kanopoulos, N., Vasanthavada, N., Baker, R.L., 1988. Design of an image edge detection filter using the sobel operator. *IEEE Journal of solid-state circuits* 23, 358–367.
- Karras, T., Aila, T., Laine, S., Lehtinen, J., 2018. Progressive growing of GANs for improved quality, stability, and variation. 6th International Conference on Learning Representations, ICLR 2018 - Conference Track Proceedings, 1–26 arXiv:1710.10196.
- Karras, T., Laine, S., Aila, T., 2019. A style-based generator architecture for generative adversarial networks. *Proceedings of the IEEE Computer Society Conference on Computer Vision and Pattern Recognition 2019-June*, 4396–4405. doi:10.1109/CVPR.2019.00453, arXiv:1812.04948.
- Kazemifar, S., Balagopal, A., Nguyen, D., McGuire, S., Hannan, R., Jiang, S., Owrangi, A., 2018. Segmentation of the prostate and organs at risk in male pelvic ct images using deep learning. *Biomedical Physics & Engineering Express* 4, 055003.
- Kazemina, S., Baur, C., Kuijper, A., van Ginneken, B., Navab, N., Albarqouni, S., Mukhopadhyay, A., 2020. Gans for medical image analysis. *Artificial Intelligence in Medicine* 109, 101938.
- Kench, S., Cooper, S.J., 2021. Generating three-dimensional structures from a two-dimensional slice with generative adversarial network-based dimensionality expansion. *Nature Machine Intelligence* 3, 299–305. URL: http://dx.doi.org/10.1038/s42256-021-00322-1https://www.scopus.com/inward/record.uri?eid=2-s2.0-85103676676&doi=10.1038%2F978-3-030-59354-4_8&partnerID=40&md5=63c4a9eec424510efdcbd66396761660, doi:10.1038/s42256-021-00322-1.
- Kirch, W. (Ed.), 2008. *Pearson’s Correlation Coefficient*. Springer Netherlands, Dordrecht. pp. 1090–1091. URL: https://doi.org/10.1007/978-1-4020-5614-7_2569, doi:10.1007/978-1-4020-5614-7_2569.
- Kniaz, V.V., Moshkantsev, P.V., Mizginov, V.A., 2020. Deep learning a single photo voxel model prediction from real and synthetic images. *Studies in Computational Intelligence* 856, 3–16. URL: https://www.scopus.com/inward/record.uri?eid=2-s2.0-85072840810&doi=10.1007%2F978-3-030-30425-6_1&partnerID=40&md5=23fd0f1f20d6a0d061de205f71e839a8, doi:10.1007/978-3-030-30425-6_1.
- Krutko, V., Belozarov, B., Budenny, S., Sadikhov, E., Kuzmina, O., Orlov, D., Muravleva, E., Koroteev, D., 2019. A new approach to clastic rocks pore-scale topology reconstruction based on automatic thin-section images and CT scans analysis, in: *Proceedings - SPE Annual Technical Conference and Exhibition*. URL: <https://www.scopus.com/inward/record.uri?eid=2-s2.0-85079117401&doi=10.2118%2F196183-ms&partnerID=40&md5=7000419208b247e67dc6d32f129e883c>, doi:10.2118/196183-ms.

- Kwon, G., Han, C., Kim, D.s., 2019. Generation of 3d brain mri using auto-encoding generative adversarial networks, in: International Conference on Medical Image Computing and Computer-Assisted Intervention, Springer. pp. 118–126.
- Ledig, C., Theis, L., Huszár, F., Caballero, J., Cunningham, A., Acosta, A., Aitken, A., Tejani, A., Totz, J., Wang, Z., Shi, W., 2017. Photo-realistic single image super-resolution using a generative adversarial network. Proceedings - 30th IEEE Conference on Computer Vision and Pattern Recognition, CVPR 2017 2017-Janua, 105–114. doi:10.1109/CVPR.2017.19, arXiv:1609.04802.
- Lei, Y., Dong, X., Tian, S., Wang, T., Patel, P., Curran, W.J., Jani, A.B., Liu, T., Yang, X., 2020a. Multi-organ segmentation in pelvic CT images with CT-based synthetic MRI, in: Progress in Biomedical Optics and Imaging - Proceedings of SPIE, p. 63. URL: <https://www.scopus.com/inward/record.uri?eid=2-s2.0-85120848763&doi=10.1117%2F12.2548470&partnerID=40&md5=8f79ad7198c491b9083a14a7a4a13ebf>, doi:10.1117/12.2548470.
- Lei, Y., Wang, T., Dong, X., Higgins, K., Liu, T., Curran, W.J., Mao, H., Nye, J.A., Yang, X., 2020b. Low dose PET imaging with CT-aided cycle-consistent adversarial networks, in: Progress in Biomedical Optics and Imaging - Proceedings of SPIE, p. 152. URL: <https://www.scopus.com/inward/record.uri?eid=2-s2.0-85086739160&doi=10.1117%2F12.2549386&partnerID=40&md5=39e2819091416fbd9184bdca4221b64>, doi:10.1117/12.2549386.
- Li, A., Du, C., Volkow, N.D., Pan, Y., 2020. A deep-learning-based approach for noise reduction in high-speed optical coherence Doppler tomography. Journal of Biophotonics 13, 1–11. URL: <https://www.scopus.com/inward/record.uri?eid=2-s2.0-85089295903&doi=10.1002%2Fjbio.202000084&partnerID=40&md5=af344492c53301aa54e3d39ec519b571>, doi:10.1002/jbio.202000084.
- Li, X., Dong, Y., Peers, P., Tong, X., 2019. Synthesizing 3D shapes from silhouette image collections using multi-projection generative adversarial networks, in: Proceedings of the IEEE Computer Society Conference on Computer Vision and Pattern Recognition, IEEE. pp. 5530–5539. URL: <https://www.scopus.com/inward/record.uri?eid=2-s2.0-85078791125&doi=10.1109%2FCVPR.2019.00568&partnerID=40&md5=2ff2125bf475391084caaea33dc4ed28>, doi:10.1109/CVPR.2019.00568, arXiv:1906.03841.
- Lin, T.Y., Goyal, P., Girshick, R., He, K., Dollár, P., 2017. Focal loss for dense object detection, in: Proceedings of the IEEE international conference on computer vision, pp. 2980–2988.
- Lin, W.W., Lin, W.W., Chen, G., Zhang, H., Gao, Q., Huang, Y., Tong, T., Du, M., 2021. Bidirectional Mapping of Brain MRI and PET With 3D Reversible GAN for the Diagnosis of Alzheimer's Disease. Frontiers in Neuroscience 15, 1–13. URL: <https://www.scopus.com/inward/record.uri?eid=2-s2.0-85104938401&doi=10.3389%2Ffnins.2021.646013&partnerID=40&md5=1d415add3bcc0ee9bdf2264a5ea172b4>, doi:10.3389/fnins.2021.646013.
- Liu, C., Kong, D., Wang, S., Li, J., Yin, B., 2021. DLGAN: Depth-Preserving Latent Generative Adversarial Network for 3D Reconstruction. IEEE Transactions on Multimedia 23, 2843–2856. URL: <https://www.scopus.com/inward/record.uri?eid=2-s2.0-85090434795&doi=10.1109%2FTMM.2020.3017924&partnerID=40&md5=856ee54b5b5a90e0f6bc37e07ed7128b>, doi:10.1109/TMM.2020.3017924.
- Liu, M., Jervis, M., Li, W., Nivlet, P., 2020a. Seismic facies classification using supervised convolutional neural networks and semisupervised generative adversarial networks. Geophysics 85, O47–O58. URL: <https://www.scopus.com/inward/record.uri?eid=2-s2.0-85095508796&doi=10.1190%2Fgeo2019-0627.1&partnerID=40&md5=e842b2b47dec1d60373a772d7f8dc154>, doi:10.1190/geo2019-0627.1.
- Liu, S., Zhong, Z., Takbiri-Borujeni, A., Kazemi, M., Fu, Q., Yang, Y., 2019. A case study on homogeneous and heterogeneous reservoir porous media reconstruction by using generative adversarial networks, in: Energy Procedia, Elsevier B.V. pp. 6164–

6169. URL: <https://www.scopus.com/inward/record.uri?eid=2-s2.0-85063896569&doi=10.1016%2Fj.egypro.2019.01.493&partnerID=40&md5=da699dd260aaf2a29d82bcaed6dab5a1https://doi.org/10.1016/j.egypro.2019.01.493, doi:10.1016/j.egypro.2019.01.493>.
- Liu, Y., Lei, Y., Wang, T., Zhou, J., Lin, L., Liu, T., Patel, P., Curran, W.J., Ren, L., Yang, X., 2020b. Liver synthetic CT generation based on dense-cyclegan for MRI-only treatment planning, in: Progress in Biomedical Optics and Imaging - Proceedings of SPIE, p. 92. URL: <https://www.scopus.com/inward/record.uri?eid=2-s2.0-85092545410&doi=10.1117%2F12.2549265&partnerID=40&md5=32566cafdde0a854df015b57d53bfab4, doi:10.1117/12.2549265>.
- Lucic, M., Kurach, K., Michalski, M., Bousquet, O., Gelly, S., 2018. Are Gans created equal? A large-scale study. Advances in Neural Information Processing Systems 2018-Decem, 700–709.
- Ma, B., Zhao, Y., Yang, Y., Zhang, X., Dong, X., Zeng, D., Ma, S., Li, S., 2020. MRI image synthesis with dual discriminator adversarial learning and difficulty-aware attention mechanism for hippocampal subfields segmentation. Computerized Medical Imaging and Graphics 86, 101800. URL: <https://www.scopus.com/inward/record.uri?eid=2-s2.0-85094326545&doi=10.1016%2Fj.compmedimag.2020.101800&partnerID=40&md5=45095a44ef52255bab9cdd79f0969ab7https://doi.org/10.1016/j.compmedimag.2020.101800, doi:10.1016/j.compmedimag.2020.101800>.
- Van der Maaten, L., Hinton, G., 2008. Visualizing data using t-sne. Journal of machine learning research 9.
- Mao, X., Li, Q., Xie, H., Lau, R.Y., Wang, Z., Smolley, S.P., 2017. Least Squares Generative Adversarial Networks. Proceedings of the IEEE International Conference on Computer Vision 2017-October, 2813–2821. doi:10.1109/ICCV.2017.304, arXiv:1611.04076.
- Mathieu, M., Couprie, C., LeCun, Y., 2016. Deep multi-scale video prediction beyond mean square error. 4th International Conference on Learning Representations, ICLR 2016 - Conference Track Proceedings , 1–14arXiv:1511.05440.
- McRobbie, D.W., Moore, E.A., Graves, M.J., Prince, M.R., 2017. MRI from Picture to Proton. Cambridge university press.
- Melitz, W., Shen, J., Kummel, A.C., Lee, S., 2011. Kelvin probe force microscopy and its application. Surface science reports 66, 1–27.
- Memon, A.R., Li, J., Egger, J., Chen, X., 2021. A review on patient-specific facial and cranial implant design using artificial intelligence (ai) techniques. Expert Review of Medical Devices 18, 985–994.
- Mirza, M., Osindero, S., 2014. Conditional Generative Adversarial Nets, 1–7URL:<http://arxiv.org/abs/1411.1784, arXiv:1411.1784>.
- Moghari, M.D., Zhou, L., Yu, B., Moore, K., Young, N., Fulton, R., Kyme, A., 2019. Estimation of full-dose 4D CT perfusion images from low-dose images using conditional generative adversarial networks, in: 2019 IEEE Nuclear Science Symposium and Medical Imaging Conference, NSS/MIC 2019, pp. 22–24. URL: <https://www.scopus.com/inward/record.uri?eid=2-s2.0-85083561421&doi=10.1109%2FNSS%2FMIC42101.2019.9059723&partnerID=40&md5=0461eac94decf3509f0319ef46f4877f, doi:10.1109/NSS/MIC42101.2019.9059723>.
- Mohamed, S., Lakshminarayanan, B., 2016. Learning in implicit generative models. arXiv preprint arXiv:1610.03483 .
- Mokhayeri, F., Kamali, K., Granger, E., 2020. Cross-Domain face synthesis using a controllable GAN, in: Proceedings - 2020 IEEE Winter Conference on Applications of Computer Vision, WACV 2020, pp. 241–249. URL: <https://www.scopus.com/inward/record.uri?eid=2-s2.0-85085470510&doi=10.1109%2FWACV45572.2020.9093275&partnerID=40&md5=09f1ff5b79bcd2ce7464daaf4c92c384, doi:10.1109/WACV45572.2020.9093275, arXiv:1910.14247>.
- Momeni, S., Fazlollahi, A., Lebrat, L., Yates, P., Rowe, C., Gao, Y., Liew, A.W.C.A.C.A.W.C., Salvado,

- O., 2021. Generative Model of Brain Microbleeds for MRI Detection of Vascular Marker of Neurodegenerative Diseases. *Frontiers in Neuroscience* 15, 1–13. URL: <https://www.scopus.com/inward/record.uri?eid=2-s2.0-85122037596&doi=10.3389%2Ffnins.2021.778767&partnerID=40&md5=0a0cdd806649cfd5335aaceab4f4d726,doi:10.3389/fnins.2021.778767>.
- Mosser, L., Dubrule, O., Blunt, M.J., 2017. Reconstruction of three-dimensional porous media using generative adversarial neural networks. *Physical Review E* 96. URL: <https://www.scopus.com/inward/record.uri?eid=2-s2.0-85032020636&doi=10.1103%2FPhysRevE.96.043309&partnerID=40&md5=3e7c29037e9983cb0debc8052c156130,doi:10.1103/PhysRevE.96.043309,arXiv:1704.03225>.
- Muzahid, A.A.M., Wanggen, W., Sohel, F., Benamoun, M., Hou, L., Ullah, H., 2021. Progressive conditional GAN-based augmentation for 3D object recognition. *Neurocomputing* 460, 20–30. URL: <https://www.scopus.com/inward/record.uri?eid=2-s2.0-85110520015&doi=10.1016%2Fj.neucom.2021.06.091&partnerID=40&md5=9cf2b7cfe7eee0c7c1ab77319c893a23https://doi.org/10.1016/j.neucom.2021.06.091,doi:10.1016/j.neucom.2021.06.091>.
- Nadipally, M., 2019. Optimization of methods for image-texture segmentation using ant colony optimization, in: *Intelligent Data Analysis for Biomedical Applications*. Elsevier, pp. 21–47.
- Navidan, H., Moshiri, P.F., Nabati, M., Shahbazian, R., Ghorashi, S.A., Shah-Mansouri, V., Windridge, D., 2021. Generative adversarial networks (gans) in networking: A comprehensive survey & evaluation. *Computer Networks* 194, 108149.
- Nozawa, N., Shum, H.P.H., Feng, Q., Ho, E.S.L., Morishima, S., 2021. 3D car shape reconstruction from a contour sketch using GAN and lazy learning. *Visual Computer* URL: <https://doi.org/10.1007/s00371-020-02024-yhttps://www.scopus.com/inward/record.uri?eid=2-s2.0-85104809946&doi=10.1007%2Fs00371-020-02024-y&partnerID=40&md5=98a68df623e1aa87f37af7bcc8d0673c,doi:10.1007/s00371-020-02024-y>.
- Olberg, S., Zhang, H., Kennedy, W.R., Chun, J., Rodriguez, V., Zoberi, I., Thomas, M.A., Kim, J.S., Mutic, S., Green, O.L., Park, J.C., 2019. Synthetic CT reconstruction using a deep spatial pyramid convolutional framework for MR-only breast radiotherapy. *Medical Physics* 46, 4135–4147. URL: <https://www.scopus.com/inward/record.uri?eid=2-s2.0-85070671134&doi=10.1002%2Fmp.13716&partnerID=40&md5=4bc934962f8f017db35f67a31a6e4593,doi:10.1002/mp.13716>.
- Pan, Y., Liu, M., Lian, C., Xia, Y., Shen, D., 2019. Disease-Image Specific Generative Adversarial Network for Brain Disease Diagnosis with Incomplete Multi-modal Neuroimages. *Lecture Notes in Computer Science (including subseries Lecture Notes in Artificial Intelligence and Lecture Notes in Bioinformatics)* 11766 LNCS, 137–145. URL: https://www.scopus.com/inward/record.uri?eid=2-s2.0-85075697955&doi=10.1007%2F978-3-030-32248-9_16&partnerID=40&md5=6a7abd8a99f5d3f6e5aa2d983262d134,doi:10.1007/978-3-030-32248-9_16.
- Pesaranghader, A., Wang, Y., Havaei, M., 2021. CT-SGAN: Computed Tomography Synthesis GAN. *Lecture Notes in Computer Science (including subseries Lecture Notes in Artificial Intelligence and Lecture Notes in Bioinformatics)* 13003 LNCS, 67–79. URL: https://www.scopus.com/inward/record.uri?eid=2-s2.0-85116943278&doi=10.1007%2F978-3-030-88210-5_6&partnerID=40&md5=c31c7bdefeeca965eb8506114b2bb261,doi:10.1007/978-3-030-88210-5_6,arXiv:2110.09288.
- Phillips, C.E., 1897. *Bibliography of X-ray Literature and Research, 1896-1897: Being a Ready Reference Index to the Literature on the Subject of Röntgen Or X-rays*. Electrician Print. and Publishing Company.
- Ponomarev, A., 2019. Fooling image copy detection algorithms with gans.
- Posilovic, L., Medak, D., Subasic, M., Petkovic, T., Budimir, M., Loncaric, S., 2021. Synthetic 3D ultrasonic scan generation using optical flow and generative adversarial networks, in: *International Symposium on Image and Signal Processing and Analysis, ISPA*, pp. 213–

218. URL: <https://www.scopus.com/inward/record.uri?eid=2-s2.0-85116974957&doi=10.1109%2FISPA52656.2021.9552069&partnerID=40&md5=2310c68b884603fe6307801bcb8c8fa6>, doi:10.1109/ISPA52656.2021.9552069.
- Qin, A., Liu, G., Chen, S., Zhao, L., Zheng, W., Yan, D., Grills, I.S., Stevens, C.W., Li, X., Ding, X., 2021. Investigate the Feasibility of Using CBCT to Assess the Dose Validation for Spot-Scanning Proton Arc (SPArc) Therapy for Advanced Staged Lung Cancer Treatment. *International journal of radiation oncology, biology, physics* 111, S98. URL: <https://www.scopus.com/inward/record.uri?eid=2-s2.0-85120929031&doi=10.1016%2Fj.ijrobp.2021.07.228&partnerID=40&md5=4dd382927a2ce8e54e06f0a2472a2c02>, doi:10.1016/j.ijrobp.2021.07.228.
- Rabin, J., Peyré, G., Delon, J., Bernot, M., 2011. Wasserstein barycenter and its application to texture mixing, in: *International Conference on Scale Space and Variational Methods in Computer Vision*, Springer. pp. 435–446.
- Ramos, D., Franco-Pedroso, J., Lozano-Diez, A., Gonzalez-Rodriguez, J., 2018. Deconstructing cross-entropy for probabilistic binary classifiers. *Entropy* 20. URL: <https://www.mdpi.com/1099-4300/20/3/208>, doi:10.3390/e20030208.
- Rosasco, L., De Vito, E., Caponnetto, A., Piana, M., Verri, A., 2004. Are loss functions all the same? *Neural computation* 16, 1063–1076.
- Rosca, M., Lakshminarayanan, B., Warde-Farley, D., Mohamed, S., 2017. Variational approaches for auto-encoding generative adversarial networks. arXiv preprint arXiv:1706.04987 .
- Ruby, U., Yendapalli, V., 2020. Binary cross entropy with deep learning technique for image classification. *Int. J. Adv. Trends Comput. Sci. Eng* 9.
- Rusak, F., Santa Cruz, R., Bourgeat, P., Fookes, C., Fripp, J., Bradley, A., Salvado, O., 2020. 3d brain mri gan-based synthesis conditioned on partial volume maps. *Lecture Notes in Computer Science (including subseries Lecture Notes in Artificial Intelligence and Lecture Notes in Bioinformatics)* 12417 LNCS, 11–20. URL: https://www.scopus.com/inward/record.uri?eid=2-s2.0-85092191503&doi=10.1007%2F978-3-030-59520-3_2&partnerID=40&md5=a014076a531da638da8f944b273ca755, doi:10.1007/978-3-030-59520-3_2.
- Russakovsky, O., Deng, J., Su, H., Krause, J., Satheesh, S., Ma, S., Huang, Z., Karpathy, A., Khosla, A., Bernstein, M., et al., 2015. Imagenet large scale visual recognition challenge. *International journal of computer vision* 115, 211–252.
- Salimans, T., Goodfellow, I., Zaremba, W., Cheung, V., Radford, A., Chen, X., 2016. Improved techniques for training gans, in: *Advances in neural information processing systems*, pp. 2234–2242.
- Sammut, C., Webb, G.I. (Eds.), 2010a. *Area Under Curve*. Springer US, Boston, MA. pp. 40–40. URL: https://doi.org/10.1007/978-0-387-30164-8_28, doi:10.1007/978-0-387-30164-8_28.
- Sammut, C., Webb, G.I. (Eds.), 2010b. *Clustering*. Springer US, Boston, MA. pp. 180–180. URL: https://doi.org/10.1007/978-0-387-30164-8_124, doi:10.1007/978-0-387-30164-8_124.
- Sammut, C., Webb, G.I. (Eds.), 2010c. *F1-Measure*. Springer US, Boston, MA. pp. 397–397. URL: https://doi.org/10.1007/978-0-387-30164-8_298, doi:10.1007/978-0-387-30164-8_298.
- Sammut, C., Webb, G.I. (Eds.), 2010d. *Mean Absolute Error*. Springer US, Boston, MA. pp. 652–652. URL: https://doi.org/10.1007/978-0-387-30164-8_525, doi:10.1007/978-0-387-30164-8_525.
- Sammut, C., Webb, G.I. (Eds.), 2010e. *Mean Squared Error*. Springer US, Boston, MA. pp. 653–653. URL: https://doi.org/10.1007/978-0-387-30164-8_528, doi:10.1007/978-0-387-30164-8_528.
- Scarfe, W.C., Farman, A.G., Sukovic, P., et al., 2006. Clinical applications of cone-beam computed tomography in dental practice. *Journal-Canadian Dental Association* 72, 75.

- Schaefferkoetter, J., Yan, J., Moon, S., Chan, R., Ortega, C., Metser, U., Berlin, A., Veit-Haibach, P., 2021. Deep learning for whole-body medical image generation. *European Journal of Nuclear Medicine and Molecular Imaging* 48, 3817–3826. URL: <https://www.scopus.com/inward/record.uri?eid=2-s2.0-85106419297&doi=10.1007%2Fs00259-021-05413-0&partnerID=40&md5=1b0a28a6c49d8915f06c6d394a3d81a1>, doi:10.1007/s00259-021-05413-0.
- Sciazko, A., Komatsu, Y., Shikazono, N., 2021. Unsupervised generative adversarial network for 3-d microstructure synthesis from 2-d image, in: *ECS Transactions*, pp. 1363–1373. URL: <https://www.scopus.com/inward/record.uri?eid=2-s2.0-85111685417&doi=10.1149%2F10301.1363ecst&partnerID=40&md5=881393f30dd1b9098d592bb479b783d7>, doi:10.1149/10301.1363ecst.
- Seitzer, M., Yang, G., Schlemper, J., Oktay, O., Würfl, T., Christlein, V., Wong, T., Mohiaddin, R., Firmin, D., Keegan, J., et al., 2018. Adversarial and perceptual refinement for compressed sensing mri reconstruction, in: *International conference on medical image computing and computer-assisted intervention*, Springer. pp. 232–240.
- Setio, A.A.A., Traverso, A., De Bel, T., Berens, M.S., Van Den Bogaard, C., Cerello, P., Chen, H., Dou, Q., Fantacci, M.E., Geurts, B., et al., 2017. Validation, comparison, and combination of algorithms for automatic detection of pulmonary nodules in computed tomography images: the luna16 challenge. *Medical image analysis* 42, 1–13.
- Shen, T., Liu, R., Bai, J., Li, Z., 2018. “deep fakes” using generative adversarial networks (gan) .
- Shen, Y., Zhang, C., Fu, H., Zhou, K., Zheng, Y., 2021. DeepSketchHair: Deep Sketch-Based 3D Hair Modeling. *IEEE Transactions on Visualization and Computer Graphics* 27, 3250–3263. URL: <https://www.scopus.com/inward/record.uri?eid=2-s2.0-85107116860&doi=10.1109%2FTVCG.2020.2968433&partnerID=40&md5=0789f45834b01ead1ce62467f8c24e12>, doi:10.1109/TVCG.2020.2968433.
- Shin, H.C., Tenenholtz, N.A., Rogers, J.K., Schwarz, C.G., Senjem, M.L., Gunter, J.L., Andriole, K.P., Michalski, M., 2018. Medical image synthesis for data augmentation and anonymization using generative adversarial networks, in: *International workshop on simulation and synthesis in medical imaging*, Springer. pp. 1–11.
- Shivegowda, M.D., Boonyasopon, P., Rangappa, S.M., Siengchin, S., 2022. A review on computer-aided design and manufacturing processes in design and architecture. *Archives of Computational Methods in Engineering*, 1–8.
- Shorten, C., Khoshgoftaar, T.M., 2019. A survey on image data augmentation for deep learning. *Journal of big data* 6, 1–48.
- Simonyan, K., Zisserman, A., 2014. Very deep convolutional networks for large-scale image recognition. *arXiv preprint arXiv:1409.1556* .
- Slossberg, R., Shamaï, G., Kimmel, R., 2019. High quality facial surface and texture synthesis via generative adversarial networks. *Lecture Notes in Computer Science (including subseries Lecture Notes in Artificial Intelligence and Lecture Notes in Bioinformatics)* 11131 LNCS, 498–513. URL: https://www.scopus.com/inward/record.uri?eid=2-s2.0-85061719627&doi=10.1007%2F978-3-030-11015-4_36&partnerID=40&md5=18e8c75d134069618fb7ab6f67d32c0a, doi:10.1007/978-3-030-11015-4_36, arXiv:1808.08281.
- Suh, S., Cheon, S., Chang, D.J.D.J., Lee, D., Lee, Y.O., 2021. Sequential Lung Nodule Synthesis Using Attribute-Guided Generative Adversarial Networks. *Lecture Notes in Computer Science (including subseries Lecture Notes in Artificial Intelligence and Lecture Notes in Bioinformatics)* 12906 LNCS, 402–411. URL: https://www.scopus.com/inward/record.uri?eid=2-s2.0-85116439173&doi=10.1007%2F978-3-030-87231-1_39&partnerID=40&md5=ba7a87a14e5ab0878799274433f5b279http://dx.doi.org/10.1007/978-3-030-87231-1_39, doi:10.1007/978-3-030-87231-1_39.
- Sun, Y., Yuan, P., Sun, Y., 2020. Mm-gan: 3d mri data augmentation for medical image segmentation via generative adversarial networks, in: *2020*

- IEEE International conference on knowledge graph (ICKG), IEEE. pp. 227–234.
- Taha, A.A., Hanbury, A., 2015. Metrics for evaluating 3d medical image segmentation: analysis, selection, and tool. *BMC medical imaging* 15, 1–28.
- Tang, Z., Zhang, D., Song, Y., Wang, H., Liu, D., Zhang, C., Liu, S., Peng, H., Cai, W., 2020. 3D Conditional Adversarial Learning for Synthesizing Microscopic Neuron Image Using Skeleton-to-Neuron Translation, in: *Proceedings - International Symposium on Biomedical Imaging*, pp. 1775–1779. URL: <https://www.scopus.com/inward/record.uri?eid=2-s2.0-85085861422&doi=10.1109%2FISBI45749.2020.9098345&partnerID=40&md5=5ee3073687dce67bda9670aade05d953>, doi:10.1109/ISBI45749.2020.9098345.
- Thanh-Tung, H., Tran, T., 2020. Catastrophic forgetting and mode collapse in gans, in: *2020 International Joint Conference on Neural Networks (IJCNN)*, IEEE. pp. 1–10.
- Ting, K.M., 2010a. *Confusion Matrix*. Springer US, Boston, MA. pp. 209–209. URL: https://doi.org/10.1007/978-0-387-30164-8_157, doi:10.1007/978-0-387-30164-8_157.
- Ting, K.M., 2010b. *Precision*. Springer US, Boston, MA. pp. 780–780. URL: https://doi.org/10.1007/978-0-387-30164-8_651, doi:10.1007/978-0-387-30164-8_651.
- Townsend, D.W., 2008. Positron emission tomography/computed tomography, in: *Seminars in nuclear medicine*, Elsevier. pp. 152–166.
- Tran, L.D., Nguyen, S.M., Arai, M., 2020. Gan-based noise model for denoising real images, in: *Proceedings of the Asian Conference on Computer Vision*.
- Wang, S., Guo, J., Zhang, Y., Hu, Y., Ding, C., Wu, Y., Approach, N., Wang, S., Guo, J., Zhang, Y., Hu, Y., Ding, C., Wu, Y., 2021. Tomosar 3d reconstruction for buildings using very few tracks of observation: A conditional generative adversarial network approach. *Remote Sensing* 13. URL: <https://www.scopus.com/inward/record.uri?eid=2-s2.0-85121325517&doi=10.3390%2Frs13245055&partnerID=40&md5=03418890e0662059d76296bc9ae162f0>, doi:10.3390/rs13245055.
- Wang, T.C., Liu, M.Y., Zhu, J.Y., Tao, A., Kautz, J., Catanzaro, B., 2018. High-resolution image synthesis and semantic manipulation with conditional gans, in: *Proceedings of the IEEE conference on computer vision and pattern recognition*, pp. 8798–8807.
- Wang, W., Huang, Q., You, S., Yang, C., Neumann, U., 2017. Shape Inpainting Using 3D Generative Adversarial Network and Recurrent Convolutional Networks. *Proceedings of the IEEE International Conference on Computer Vision 2017-October*, 2317–2325. URL: <https://www.scopus.com/inward/record.uri?eid=2-s2.0-85039427576&doi=10.1109%2FICCV.2017.252&partnerID=40&md5=516fe973827c8cea2ba96767e254325c>, doi:10.1109/ICCV.2017.252, arXiv:1711.06375.
- Wang, Z., Bovik, A.C., Sheikh, H.R., Simoncelli, E.P., 2004. Image quality assessment: from error visibility to structural similarity. *IEEE transactions on image processing* 13, 600–612.
- Wang, Z., Simoncelli, E.P., Bovik, A.C., 2003. Multi-scale structural similarity for image quality assessment, in: *The Thrity-Seventh Asilomar Conference on Signals, Systems & Computers, 2003*, Ieee. pp. 1398–1402.
- Weber, M., Fürst, M., Zöllner, J.M., 2020. Automated focal loss for image based object detection, in: *2020 IEEE Intelligent Vehicles Symposium (IV)*, IEEE. pp. 1423–1429.
- Wei, R., Liu, B., Zhou, F., Bai, X., Fu, D., Liang, B., Wu, Q., 2020. A patient-independent CT intensity matching method using conditional generative adversarial networks (cGAN) for single x-ray projection-based tumor localization. *Physics in Medicine and Biology* 65. URL: <https://www.scopus.com/inward/record.uri?eid=2-s2.0-85089846140&doi=10.1088%2F1361-6560%2Fab8bf2&partnerID=40&md5=454c6fcade0705e9f2cef292ae76696c>, doi:10.1088/1361-6560/ab8bf2.
- Wu, Z., Lischinski, D., Shechtman, E., 2021. StyleSpace analysis: Disentangled controls for

- stylegan image generation, in: Proceedings of the IEEE/CVF Conference on Computer Vision and Pattern Recognition, pp. 12863–12872.
- Xu, Z., Wang, X., Shin, H.C., Roth, H., Yang, D., Milletari, F., Zhang, L., Xu, D., 2019. Tunable CT lung nodule synthesis conditioned on background image and semantic features. Lecture Notes in Computer Science (including subseries Lecture Notes in Artificial Intelligence and Lecture Notes in Bioinformatics) 11827 LNCS, 62–70. URL: https://www.scopus.com/inward/record.uri?eid=2-s2.0-85075660630&doi=10.1007%2F978-3-030-32778-1_7&partnerID=40&md5=ac5711e8b1c5bb8abc6d3fef003417ca, doi:10.1007/978-3-030-32778-1_7.
- Yan, Y., Lee, H., Somer, E., Grau, V., 2018. Generation of Amyloid PET Images via Conditional Adversarial Training for Predicting Progression to Alzheimer’s Disease. volume 1. Springer International Publishing. URL: http://dx.doi.org/10.1007/978-3-030-00320-3_4, doi:10.1007/978-3-030-00320-3_4.
- Yang, B., Wen, H., Wang, S., Clark, R., Markham, A., Trigoni, N., 2017. 3D Object Reconstruction from a Single Depth View with Adversarial Learning, in: Proceedings - 2017 IEEE International Conference on Computer Vision Workshops, ICCVW 2017, pp. 679–688. URL: <https://www.scopus.com/inward/record.uri?eid=2-s2.0-85039414245&doi=10.1109%2FICCVW.2017.86&partnerID=40&md5=aa8388dd5ee37ec22a034f1daf586de1>, doi:10.1109/ICCVW.2017.86, arXiv:1708.07969.
- Yang, C., Eschweiler, D., Stegmaier, J., 2021a. Semi- and Self-supervised Multi-view Fusion of 3D Microscopy Images Using Generative Adversarial Networks. Lecture Notes in Computer Science (including subseries Lecture Notes in Artificial Intelligence and Lecture Notes in Bioinformatics) 12964 LNCS, 130–139. URL: https://www.scopus.com/inward/record.uri?eid=2-s2.0-85116937914&doi=10.1007%2F978-3-030-88552-6_13&partnerID=40&md5=ea265b6f990759e10bc9b0af62845ccc, doi:10.1007/978-3-030-88552-6_13, arXiv:2108.02743.
- Yang, D., Liu, B., Axel, L., Metaxas, D., 2019. 3D LV Probabilistic Segmentation in Cardiac MRI Using Generative Adversarial Network. Lecture Notes in Computer Science (including subseries Lecture Notes in Artificial Intelligence and Lecture Notes in Bioinformatics) 11395 LNCS, 181–190. URL: http://dx.doi.org/10.1007/978-3-030-12029-0_20https://www.scopus.com/inward/record.uri?eid=2-s2.0-85064048751&doi=10.1007%2F978-3-030-12029-0_20&partnerID=40&md5=df0c44c6e64d1af853a0760ebc220de7, doi:10.1007/978-3-030-12029-0_20.
- Yang, H., Lu, X., Wang, S.H.S.H.S.H., Lu, Z., Yao, J., Jiang, Y., Qian, P., 2021b. Synthesizing Multi-Contrast MR Images Via Novel 3D Conditional Variational Auto-Encoding GAN. Mobile Networks and Applications 26, 415–424. URL: <https://www.scopus.com/inward/record.uri?eid=2-s2.0-85094113961&doi=10.1007%2Fs11036-020-01678-1&partnerID=40&md5=bd7e299a87a4a46e73d1b03c491d3184>, doi:10.1007/s11036-020-01678-1.
- Yi, X., Walia, E., Babyn, P., 2019. Generative adversarial network in medical imaging: A review. Medical image analysis 58, 101552.
- Zeng, G., Zheng, G., 2019. Hybrid generative adversarial networks for deep MR to CT synthesis using unpaired data. Lecture Notes in Computer Science (including subseries Lecture Notes in Artificial Intelligence and Lecture Notes in Bioinformatics) 11767 LNCS, 759–767. URL: https://www.scopus.com/inward/record.uri?eid=2-s2.0-85075656912&doi=10.1007%2F978-3-030-32251-9_83&partnerID=40&md5=40bf9291e5e5a750fd7031d3f4cf6212, doi:10.1007/978-3-030-32251-9_83.
- Zhang, H., Sindagi, V., Patel, V.M., 2019a. Image de-raining using a conditional generative adversarial network. IEEE transactions on circuits and systems for video technology 30, 3943–3956.
- Zhang, H., Xu, T., Li, H., Zhang, S., Wang, X., Huang, X., Metaxas, D.N., 2017. Stackgan: Text to photo-realistic image synthesis with stacked generative adversarial networks, in: Proceedings of the IEEE international conference on computer vision, pp. 5907–5915.

- Zhang, Z., Yang, L., Zheng, Y., 2018. Translating and Segmenting Multimodal Medical Volumes with Cycle- and Shape-Consistency Generative Adversarial Network, in: Proceedings of the IEEE Computer Society Conference on Computer Vision and Pattern Recognition, IEEE. pp. 9242–9251. URL: <https://www.scopus.com/inward/record.uri?eid=2-s2.0-85058783644&doi=10.1109%2FCVPR.2018.00963&partnerID=40&md5=a0749e6db0e9fc14f591a72c5c3fd996>, doi:10.1109/CVPR.2018.00963, arXiv:1802.09655.
- Zhang, Z., Yang, L., Zheng, Y., 2019b. Multimodal medical volumes translation and segmentation with generative adversarial network. Elsevier Inc. URL: <https://www.scopus.com/inward/record.uri?eid=2-s2.0-85082616626&doi=10.1016%2FB978-0-12-816176-0.00013-2&partnerID=40&md5=21cfc89414450ca38207cbb90205952ahttps://doi.org/10.1016/B978-0-12-816176-0.00013-2>, doi:10.1016/B978-0-12-816176-0.00013-2.
- Zhang, Z., Zhao, T., Gay, H., Zhang, W., Sun, B., 2021. Semi-supervised semantic segmentation of prostate and organs-at-risk on 3D pelvic CT images. Biomedical Physics and Engineering Express 7. URL: <https://www.scopus.com/inward/record.uri?eid=2-s2.0-85117199613&doi=10.1088%2F2057-1976%2Fac26e8&partnerID=40&md5=c07dd90ced285901aeb3ac98c05b41b4>, doi:10.1088/2057-1976/ac26e8.
- Zhou, T., Fan, D.P., Cheng, M.M., Shen, J., Shao, L., 2021. Rgb-d salient object detection: A survey. Computational Visual Media 7, 37–69.
- Zhu, J.Y., Park, T., Isola, P., Efros, A.A., 2017. Unpaired image-to-image translation using cycle-consistent adversarial networks, in: Computer Vision (ICCV), 2017 IEEE International Conference on.
- Zhuang, P., Schwing, A.G., 2019. Fmri data augmentation via synthesis. 2019 IEEE 16th International Symposium on Biomedical Imaging (ISBI 2019) , 1783–1787.
- Zollhöfer, M., Stotko, P., Görlitz, A., Theobalt, C., Nießner, M., Klein, R., Kolb, A., 2018. State of the art on 3d reconstruction with rgb-d cameras, in: Computer graphics forum, Wiley Online Library. pp. 625–652.